Evolution of squall line variability and error growth in an ensemble of LES

Edward Groot[1] and Holger Tost[1]

[1]Institut für Physik der Atmosphäre, Johannes Gutenberg Universität, Johannes-Joachim-Becher-Weg 21, Mainz, Germany

Correspondence: Edward Groot (egroot@uni-mainz.de)

Abstract. A chain of processes is identified that regulates much of the ensemble spread in an ensemble of squall lines in large eddy simulations with tight initial conditions. Patterns of gravity wave propagation decorrelate and restructure the initial condition spread until a second phase of convective initiation, after 30 minutes of simulation time. Subsequently, variability in this convective initiation and mass overturn is associated with cold pool acceleration within the ensemble envelope (propagation at 2-4 m/s).

An ensemble sensitivity analysis reveals that anomalies in squall line relative flow with respect to the ensemble mean are also associated with the secondary convective initiation. Downdrafts are fed with extra air by a convergence zone on the rearward flank of the updrafts. An analysis of difference growth within the ensemble shows that a substantial proportion of variability is explained by cold pool propagation contrasts during this stage (30-80 minutes), which is partly removed when a feature relative perspective is taken. The patterns of coherent variability exist on the time scale of an hour and dissipate subsequently (80-100 minutes).

1 Introduction

Squall lines are complex meteorological phenomena consisting of an elongated linear area with convective cells that usually induce a coherent mesoscale circulation. They often develop into mixed stratiform-convective precipitation systems with spatial extents of up to several hundred kilometers in the horizontal and a lifetime exceeding several hours. Squall lines are an active research field since several decades (Houze, 2004, 2018).

Given the increasing computational resources, high resolution simulations in convective studies have become feasible nowadays. Throughout the last 25 years, simplified cloud resolving km-scale simulations (Weisman et al., 1997) can be augmented by systematic sets of fully three dimensional large eddy simulations (LES) at hight resolutions (Adams-Selin, 2020a, b). This allowed for an improved understanding of the impact of shear profiles and resulting convective organisation (e.g. Weisman and Rotunno, 2004; Coniglio et al., 2006; Adams-Selin, 2020a), including squall line organisation. It also includes the aspect of representation: the model impact of resolution on squall line evolution and associated convergence at (sufficiently) high resolution (Weisman et al., 1997; Bryan et al., 2003; Lebo and Morrison, 2015). Bryan et al. (2003) found that even LES simulations do not result in true convergence of solutions, as the needs for parameterising processes shifts to subgrid turbulence in a partly represented inertial subrange and microphysics. How squall lines depend on microphysics, shear and instability has

been investigated rigorously by now, (e.g. Morrison et al., 2009; Grant et al., 2018; Adams-Selin, 2020a, b).

Squall line ensembles and their error growth have been investigated by Melhauser and Zhang (2012); Hanley et al. (2013); Weyn and Durran (2017). Individual ensemble members were compared to each other with a focus on the differences in their evolution.

Application of the word "error" and similar terms ("intrinsic limit") to ensemble differences requires a perfect model assumption or a perfect error assumption (e.g. Selz, 2019): the physics of errors has to be assumed to be represented perfectly in a numerical model, which is reasonable at $> 7\Delta x$, but not at smaller scales (Skamarock, 2004). Melhauser and Zhang (2012) and Hanley et al. (2013) looked at a set of simulations featuring a real squall line case in a local area model from the larger mesoscale and synoptic point of view. This was the core feature of both sensitivity studies, even though downscale "contamination" from the synoptic scale was present and considered. Melhauser and Zhang (2012) found that an intrinsic limit of predictability can affect squall line ensemble forecasts: by reducing initial condition spread by a factor of 8, their simulations could still diverge about as much as with unreduced initial condition spread. Furthermore, the contingency of convective initiation was found to be a key for the ensemble spread. Some very similar results were found by Hanley et al. (2013).

Weyn and Durran (2017) have looked at error growth in mesoscale convective systems with squall line like features in isolation. The simulations of Weyn and Durran (2017) had a resolution of 1 km on a domain with horizontal scales of about 500 km. Most of their error growth analysis was done from the spectral point of view, which implies that there was much less attention on convective and accompanying processes in physical space. Despite this focus they have compared the error growth of divergent and rotational wind components and found that divergent winds are mostly affecting larger scale errors. Furthermore, an important finding was that by reducing initial condition spread by factors of 5 and 25, only about 1 hour of predictability was won. Compared to their saturation time scale of about 5 hours this is not much.

In this study, sensitivity analyses will be carried out from a dynamical point of view with squall line simulations in isolation from a synoptic and larger mesoscale environment. Error growth will be analysed in high resolution simulations (200 m) with 10 ensemble members. The dynamical aspects that will be analysed are the following, including a short review for each of them respectively:

- **Gravity wave dynamics**

  Interaction between gravity wave dynamics and a convective environment has been investigated using a linear gravity wave model (Bretherton and Smolarkiewicz, 1989; Nicholls et al., 1991; Mapes, 1993). The latter argued that propagation of the gravity waves is important for upscale organisation of convective systems as it happens in the tropics. In these studies a heating signal was used as a proxy for a convective system, mimicking the latent heating source. Subsequently, cloud models have been used to investigate how gravity wave dynamics can concentrate regions of upward motion, with several vertical gravity wave modes favoring certain regions of convective initiation that can subsequently assist to form coherent patterns and upscale organisation (e.g. Lane and Reeder, 2001; Stechmann and Majda, 2009; Adams-Selin and Johnson, 2013; Lane and Zhang, 2011; Grant et al., 2018, and references in the latter two). In addition, Bierdel et al. (2017) have created a model for better understanding of the error propagation from convective scales to

large mesoscales and (sub-)synoptic scales caused by differences in convective heating based on the linear gravity wave model (Bretherton and Smolarkiewicz, 1989; Nicholls et al., 1991), but focusing on the role of rotation on these scales and geostrophic adjustment of difference flow. That scale is substantially larger than (sub-)squall line scales investigated here.

– **Convective initiation**

Looking from the convective initiation point of view, Fovell et al. (2006) showed how gravity waves affect squall line regions on smaller scales. In their simulations with explicitly resolved deep convection, it was shown how gravity waves can trigger initiation of discrete convective cells ahead of a squall line, that can subsequently merge with the main system. A sensitivity of these discrete convective cell was identified, which lead to a dependence of initiation on the active treatment of radiation. The sensitivity of convective initiation has played an important role in Melhauser and Zhang (2012); Adams-Selin (2020a, b) and can nowadays be resolved more accurately due to finer grid spacing.

– **Cold pool relative motion, or more specifically u in x-z plane averaged along squall lines**

Pandya and Durran (1996) have looked at the (sub)system scale variability explained by thermally forced gravity waves and found that the mesoscale squall line circulation in their system depends to a large extent on the magnitude and shape of thermal forcing. Low level features, notably the rear inflow jet, depend on the low level conditions, especially N^2. Their study has a strong focus on the squall line system circulation (u) in the plane perprendicualar to the squall line orientation and it also assesses the impact of modified physical processes on that flow.

– **Updraft and downdraft motion**

Updraft and downdraft characteristics can be sensitive to resolution and that may lead to biases in updrafts (or downdrafts) when a comparison to radar images is made (e.g. Varble et al., 2020; Lebo and Morrison, 2015; Varble et al., 2014), which could propagate to other aspects of squall line simulations (Varble et al., 2020, 2014). However, since no comparison between simulations at different resolutions or observations and simulations is made here, such sensitivities are not applicable. Furthermore, the grid spacing is believed to be fine enough for accurately resolving updraft and downdraft characteristics (Bryan et al., 2003; Lebo and Morrison, 2015; Varble et al., 2020).

This study is restricted to the analysis of one idealised squall line case with weak ensemble perturbations. Furthermore, the squall line evolution is initially nearly two dimensional due to the nearly 2D flow and initial conditions. However, this nearly 2D structure is of benefit for the analysis of squall line relative flow. Considering just one case also allows for detailed consideration of the dynamical aspects listed. The magnitude of ensemble perturbations that are applied are equivalent to a vertical wind profile uncertainty of about or less than one model layer in the vertical in typical convection permitting models. Altogether the aim is to get a comprehensive overview of the processes in which errors are showing up in a high resolution squall line ensemble, following such a small initial condition perturbation. We also describe how these errors may be transferred from one process to another. Furthermore, intrinsic predictability can be addressed, given the small magnitude of initial condition perturbations. Zonal shear in a shallow layer is perturbed with magnitudes of 0-5% and randomly, as opposed to the often used

systematic iterative approaches (e.g. Selz, 2019; Zhang et al., 2019; Selz et al., 2022; Melhauser and Zhang, 2012).

In this study, some analysis techniques are applied which are not so commonly used in studies of mesoscale convective systems. Next to more widely used passive tracers (e.g. Grant et al., 2018), an ensemble sensitivity analysis (Hanley et al., 2013; Torn and Romine, 2015; Bednarczyk and Ancell, 2015, but the latter with parameterized convection) and a difference kinetic energy metric are used. Passive tracers are an important tool to identify variability in convective transport, but by targeting at an inflow layer, contrasts can be identified early on. Variability in a secondary phase of convective initiation is revealed this way. In combination with tailored ensemble sensitivity analysis which allows to connect the strength of the convective initiation with subsequent evolution of the squall line circulation (u), the effects of this phase of initiation can be followed in time. System relative flow is evaluated and its relation with secondary convective initiation is analysed. The difference kinetic energy error growth metric and specific diagnostics can provide further insights in the evolution of system relative motion and its role in error growth (Zhang, 2005; Zhang et al., 2007).

In Section 2 the characteristics of the simulations are documented, as well as the initial conditions and ensemble design. Furthermore, the general region and time windows of focus are pointed out and the statistical verification techniques are described. In Section 3 the main analysis is carried out, preceded by a description of diagnostics used in a subsection. The section starts with a general evolution of the simulated squall line echoes. After looking at the simulated radar reflectivities, the comparison section (Section 3.2) describes secondary convective initiation and identifies a relation with gravity wave signals. This is followed by an investigation of the cold pool propagation (Section 3.3.1). Then ensemble sensitivity analysis (Section 3.3.2) assesses the connection with the squall line relative flow, followed by an investigation of downdrafts and additional statistical considerations (Section 3.3.3). Section 3 ends with an error growth (Section 3.4) analysis in grid point space and a system relative flow feedback to highlight associated contrasts in error growth. The set of analyses is synthesized in Section 4, followed by a discussion (also in that section). This discussion leads to the conclusions, as given in Section 5.

2 Methods

2.1 Model configuration

Experiments are conducted with the cloud resolving model CM1 on a 120 by 120 km grid with a depth of 20 km and duration of 2 hours simulation time, using the model version of Bryan (2019). The time steps are 0.75 s, with output stored every 5 minutes. All grid cells have a 200 m horizontal grid spacing and 100 m in the vertical. The upper 5 kilometers of the domain consists of a sponge layer with damping that absorbs upward propagating gravity wave signals. CM1 is running in the large eddy simulation mode, where the subgrid turbulence model is handled with a TKE-scheme after Deardorff (1980). The default CM1 microphysics scheme is used, which is the 2 moment Morrison scheme with hail (Morrison et al., 2009), namely its version 3.6 - with resolved supersaturation and condensation based on saturation adjustment (see also Morrison et al., 2005). The advection scheme applies a 5th order advection algorithm and Coriolis acceleration is ignored. Radiation is not actively resolved. All simulations use the same aforementioned settings.

The boundary conditions are non-periodic in all directions, which leads to the theoretical availability of an infinite reservoir of inflow air. Derivatives of all quantities are set to 0 at the boundaries. Wave signals can therefore partially reflect at the boundaries. To reduce effects of boundary reflections, the outer regions on the north and south ends of the squall line are excluded from the main analysis framework. More details and download instructions for the namelist file and output data of all simulations can be found in the setup and namelist material at https://tinyurl.com/groot-tost-22 (Groot, 2022).

2.2 Environmental conditions and ensemble perturbations

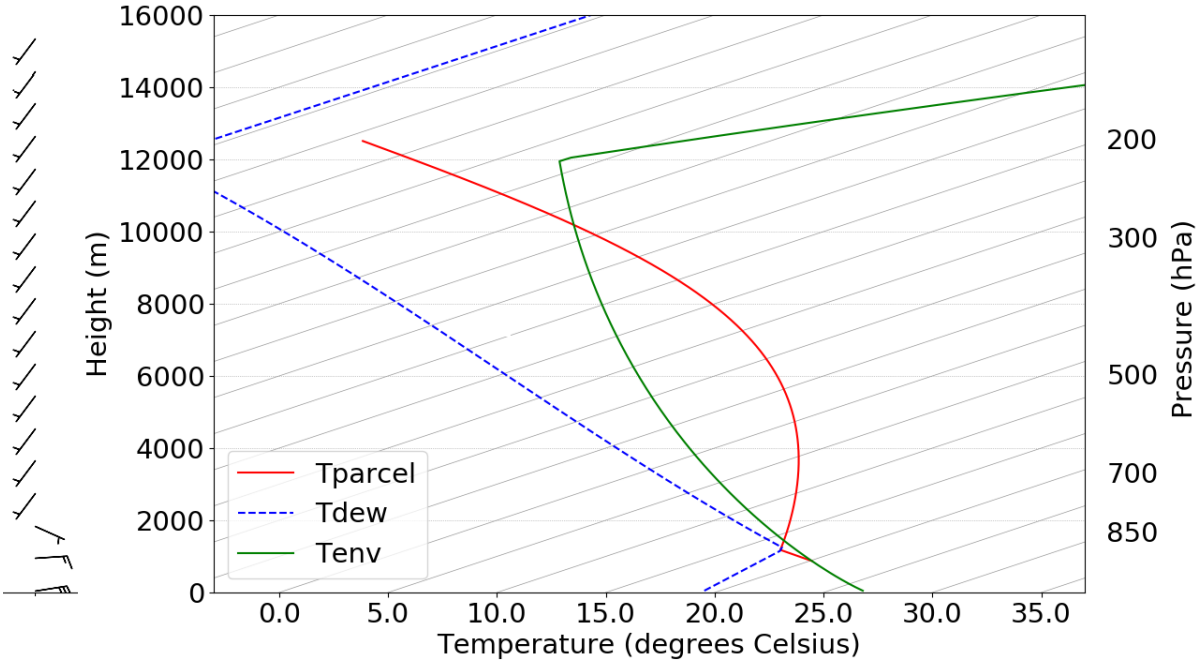

Figure 1. Thermodynamical profile based on Weisman and Klemp (1982) and wind profile after Rotunno et al. (1988), with adjustments. Temperature: green solid line; dew point: blue dashed line; convectively lifted undiluted parcel's temperature: red line. The parcel is initially lifted from the mixed layer, at $z = 900$ m.

The thermodynamic profile in each of the simulations is based on Weisman and Klemp (1982) (Figure 1), which represents the conditions in the eastern half of the domain at $t = 0$ minutes.

Below $z = 2500$ m, a potential temperature perturbation that decreases linearly in magnitude with z from -6 K at the surface to 0 at 2500 m is set at initial time for the western half of the domain, $x < 0$ km. The contrast between these two air masses triggers upward motion at their interface ($x = 0$ km) and the given environment leads to a convectively very unstable environment with a CAPE of about 2000 J/kg for rising warm air mass in the east. The convectively very unstable initial conditions associated with the Weisman and Klemp (1982) sounding are selected on purpose: the aim of this study is to analyse the behaviour of an ensemble spread of a squall line (when the development of a squall line is given) through the development of small deviations

within the squall line. This perspective complements that of Melhauser and Zhang (2012), in which the criticality of first generation convective initiation itself is explored.

The basic character of the wind profile is sheared and adjusted from Rotunno et al. (1988), with the u-component linearly varying from 12.5 m/s easterly inflow at the surface to weak westerly flow of 1.5 m/s above the top of the shear layer (Figure 1). That top of the shear layer is set at $z_{i,ref} = 2500$ m for the reference simulation. The v-component of the wind varies linearly from -2 (surface) to +2 m/s ($z \geq z_i$) over the same layer. The latter is needed to develop some three dimensionality in the simulation. Given fully 2D initial conditions, the three dimensionality could have been absent without any differential meridional advection in combination with the open boundary conditions. Given that wind profile, the shear vectors are nearly perpendicular to the initial cold pool boundary. In combination with the strong convective instability near the interface, it leads to the formation of a squall line.

Note that the wind profile implies the omission of deeper shear, which on average reduces the depth of vertical displacements and the size of convective systems (Coniglio et al., 2006). This is beneficial for a reduction of the storm relative flow and hence to reduce the across line growth of the squall lines: their residence time within the domain is increased.

An ensemble is generated by randomly perturbing the interface height (z_i), with a maximum absolute deviation from the reference height $z_{i,ref}$ of -127 m (5%) for ENS-05 $z_{i,ENS-05}$ among the 9 randomly drawn perturbed interface heights $z_{i,ENS-X}$ and a mean absolute deviation of 67 m (2.7%) from $z_{i,ref}$ (see also Groot, 2022). These perturbed interface heights are then translated to the equivalent zonal and meridional velocities by linear interpolation below the perturbed interface and constant winds above at the model grid (vertically equidistant at 100 m intervals) to obtain the final perturbations. The magnitude of perturbations is equivalent to about one model level in high resolution models, effectively an extension or shrinkage of the sheared layer is achieved with these perturbations. However, the cold pool depth and hence the potential energy distribution is not affected by the ensemble perturbations; thus, the kinetic energy distribution of the initial conditions shows only weak deviations located at low levels within the ensemble.

2.3 Spatial and temporal windows for diagnostics

Presented diagnostics are applied to a central portion of the squall line region, where 40 km$> y > -20$ km. This is to reduce the effects of the boundaries and their wave reflections on the analysis of the squall line evolution. Generally, boundary effects in the central part of the domain become only notable during the last 30-40 minutes of the simulation. Furthermore, the ensemble members all have slightly different boundary conditions, as controlled by their own evolution nearby/at the boundaries. The boundary conditions are solely based on their conditions, with the first derivatives set to zero right at the boundary. Therefore these are initially inherited by z_i as much as their whole difference evolution to the control or ensemble mean is essentially controlled by the initial value of z_i. In the x-direction a region within 1 km of the boundaries is excluded from the analysis.

Some analyses (ensemble sensitivity analysis; Section 3.3.2 and the error growth analysis of Section 3.4) are carried out relative to the *cold pool edge*, of which the detection is described later in Section 3.3.1.

This study focusses on the evolution up to 75-80 minutes of the simulations. Nevertheless, the last 40 minutes of simulation time are also taken into account.

2.4 Statistical assessment of the robustness of signals

To determine the robustness of the analysed signals given the small ensemble size ($n = 10$), a statistical test citerion based on a t-test has been defined. With the given ensemble size, correlation coefficients exceeding $|r| > 0.631$ are significant at α of 0.05. That means their frequency of occurrence in any large random sample is expected to be about 5% at $p = 0.05$ and 1.25% for random occurrence of $|r| > 0.75$ ($p = 0.0125$).

In this study, statistical grid point testing will be applied to spatial patterns within the squall line to determine a statistically significant signal. This is achieved in case of a significant correlation of a certain feature of interest with a large fraction of the grid points located within its area. In the limit case this fraction f needs to theoretically fulfill a criterion close to $f > 2p$ (Wilks, 2016). On the contrary, other features without signals associated with it would simultaneously reveal small fractions of grid points with statistical significance. This is valid most of the signals in the stratosphere (z of $15 - 20$ km) for instance. If fully random, a significant area fraction f of about 0.05 is expected, with $f \leq 2p = 0.1$ for $p = 0.05$ and 0.025 for $p = 0.0125$.

3 Results

3.1 Evolution of squall line radar reflectivity

As an overview of the general properties and behavior of a squall line (one ensemble member with strong squall line development is selected), the evolution of the simulated radar reflectivity is discussed. Reflectivity calculations in the used scheme (Morrison et al., 2009) are based on the assumption of a 10 cm wavelength with light undergoing Rayleigh scattering by cloud ice, water and mixtures of those, integrating the water mass (Bryan, 2019).

3.1.1 Squall line evolution (one member example)

As a response to the (1) large latent instability, (2) relatively strong low level wind shear perpendicular to the cold pool and the (3) strong forcing of upward motion by the cold pool, deep convection soon develops along the full length of the y-axis. Narrow echoes of about 40 dBz right above the initial condition "discontinuity" at $x = 0$ km appear after 15 minutes into the simulation (Figure 2a). About five to ten minutes later echoes exceeding 20 dBz reach above $z = 10$ km, as can be deduced from Figure 2c and 2d. Echoes also widen and exceed 60 dBz in the core region of the line. For the following 30 minutes, the squall line echoes grow monotonically at both anvil level and low/mid level. The increase in areas with reflectivity $> 20dBz$ occurs both upshear and downshear of the convective core (as could be deduced from Figures 2g, h), which itself is more or less stationary above $x = 0$ km. However, then the growth halts for a while on the downshear side after about one hour and on the upshear side after about 75 minutes (Figure 2k). Some shrinkage of the areas with substantial cloud reflectivity occurs. After 80-90 minutes a stratiform region of precipitation starts to develop on the upshear flank of the system (Figure 2j) and the anvil expands in both directions toward the end of the simulation, growing to about 100 km length, which is nearly the full domain. However, the stratiform precipitation area remains rather restricted to a very limited region at the rear flank (Figure 2j, at 3 km) and precipitation intensities remain rather low.

Starting from initial conditions that depend on x and z but not on y, initially the system is obviously nearly homogeneous in y (see Figure 2). The system gradually develops into a 3D squall line. Gradients develop along the y-axis with convective cells of higher reflectivity embedded within the line after 50 minutes and beyond this time. However, we will mostly focus on results averaged in the y-direction, as contrasts are largest in x- and z-directions and tend to be smoother along the y-axis.

3.1.2 Secondary phase of convective initiation

In Figure 2 the evolution of the squall line in ensemble member 3 is shown. From the convective point of view, this member is on the very active end of the ensemble distribution. Within the first 30 minutes of the simulations, ensemble variation is barely detectable.

Upon this mature stage of the first line of cells follows a phase were secondary initiation happens at $t = 30$ to 40 minutes. This secondary phase of convective initiation is most distinctive in ensemble member 3, where a secondary line of cells is triggered just ahead of the former line of cells and leads to forward displacements of the squall line core. The reflectivity at $t = 50$ minutes clearly illustrates the forward displacement of convective cells and an increased area of reflectivity > 55 dBz on the forward flank when the evolution of ensemble member 3 (ENS-03; Figure 2e) is compared with the reference run (Figure 2f). The reference run is basically not supporting the development of the secondary phase of initiation and hence the squall line appears to be practically stagnant until $t = 50$ minutes (Figure 2f). If any of the echoes in the reference simulation reach $x > 5$ km, it is anvil precipitation with reflectivity that locally reaches about 40 dBz just below melting level, as opposed to newly initiated updrafts with reflectivities reaching 55-65 dBz for some cells (Figure 2).

Following upon the secondary phase of convective initiation, the line of cells starts accelerating eastward, with the reflectivity signals exceeding 45 dBz at $z = 3$ km propagating to $x = 10$ km after 75 minutes and almost $x = 15$ km after 100 minutes (ENS-03). The line becomes increasingly inhomogeneous in the y-direction and exceeds 45 dBz at $z = 3$ km (about a km below melting level) over a longitudinal stretch of 15-20 km during this period, with very intense cores of 65 dBz. The latter is obviously the consequence of the low level cold pool in combination with about 2000 J/kg CAPE (see Weisman and Klemp, 1982) and 14-15 m/s of wind shear over the lower 2.5 km. These are favorable conditions for very intense linear convection.

3.2 Detailed comparison of two example simulations

This section compares the two ensemble members (mentioned above; ensemble member 3 with strong secondary initiation and the reference simulation, see also Figure 2) in detail, because they appear at opposite ends of the distributions in most diagnostics. The evolution of convergence and divergence zones in space and time is described (Section 3.2.1). Describing their motion is needed to understand how the sources and sinks of convective updrafts displace with time.

Passive tracers in the simulation pair are analysed in Section 3.2.2 for further analysis of the contrasts between the two simulations.

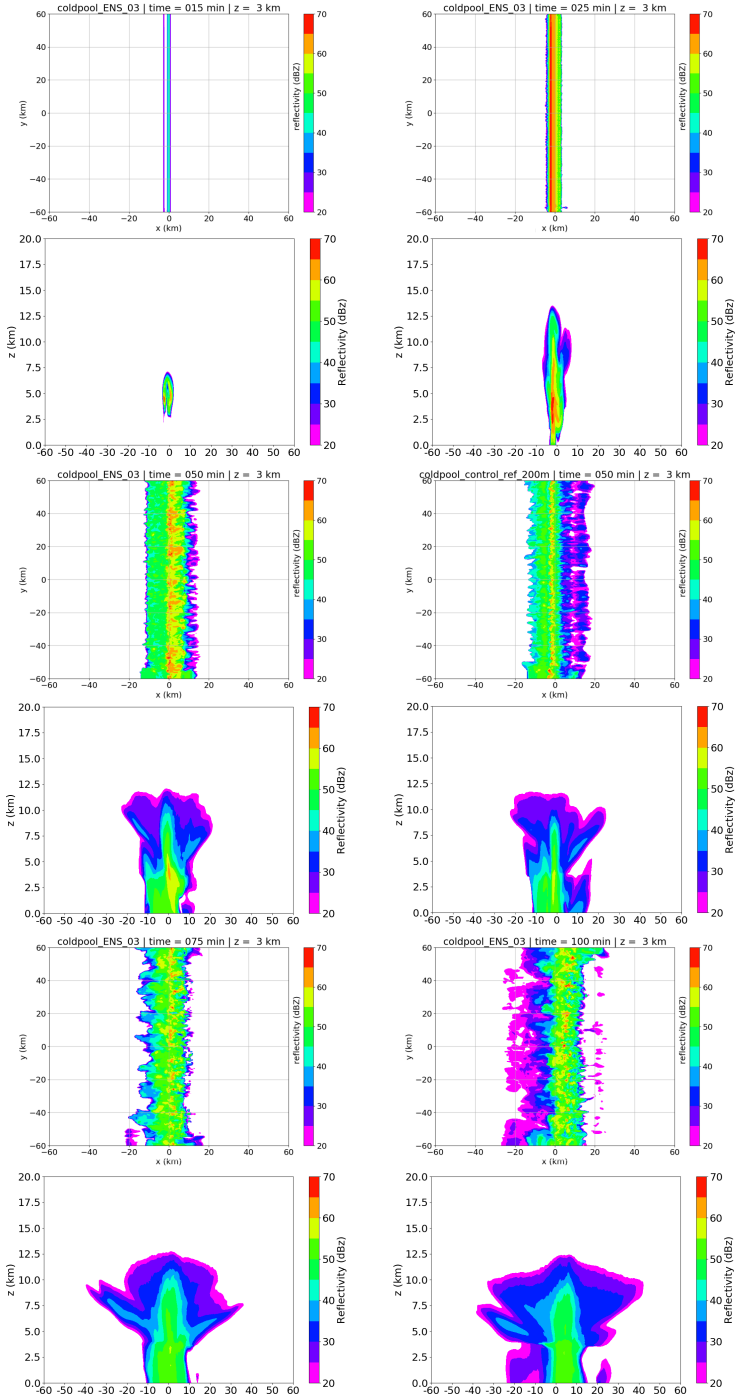

Figure 2. Evolution of simulated reflectivity for ensemble member 3 and the reference simulation (only $t = 50$ minutes) at $z = 3$ km. A horizontal cross section is followed by corresponding x-z cross section directly below, with median reflectivity along the squall line. Left top (a,c): $t = 15$ minutes, right top (b,d): $t = 25$ minutes, left center (e,g): $t = 50$ minutes (ensemble member 3), right center (f,h) $t = 50$ minutes (reference simulation), left bottom (i,k): $t = 75$ minutes, right bottom (j,l): $t = 100$ minutes.

3.2.1 Convergence and divergence zones

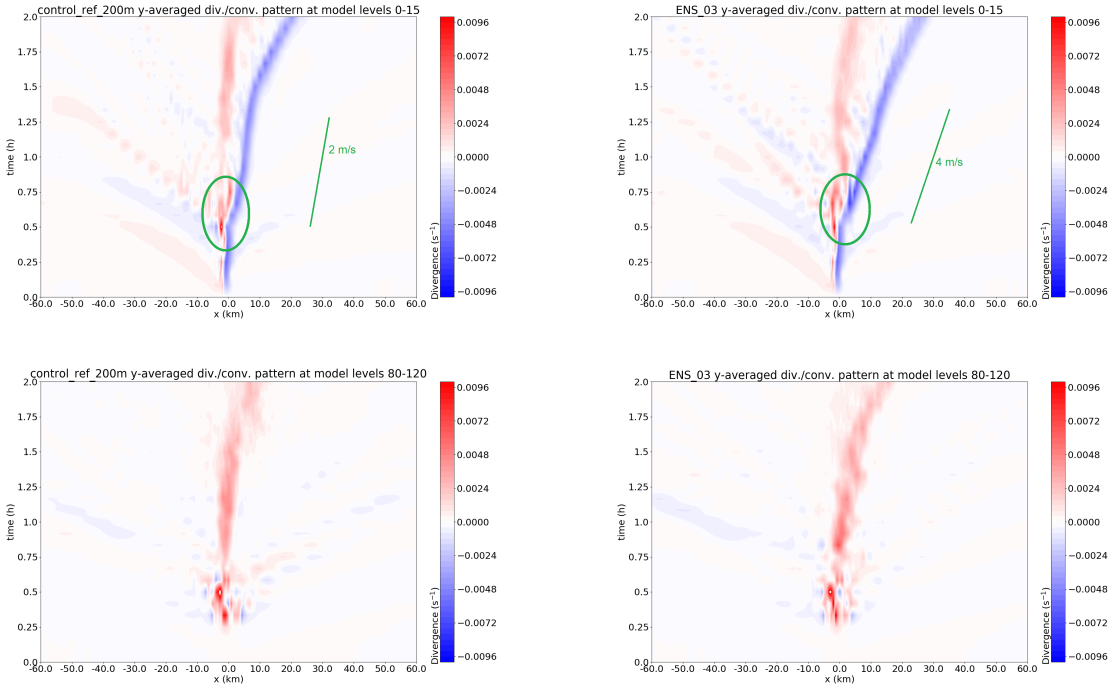

Figure 3. Space-time distribution of low level (0-1.5 km; top) and upper tropospheric (8-12 km; bottom) convergence (s^{-1}) features in the reference simulation (left) and ensemble member 3 (right), averaged over all y and given z. A stage of particular interest that is analysed in the text is highlighted with a green oval, as well as the slope of the convergence zones halfway the simulation.

Figure 3 shows a set of Hovmöller-like diagrams of divergence (red colors) and convergence (blue colors) in the lower and upper troposphere. The upper row panels depict that the low level convergence zone accelerates eastward in both simulations after a nearly stagnant position in approximately the first 30 minutes. This is in agreement with the displacement of convective cells as described in the previous section (Section 3.1). After this stagnant stage, several patterns indicating eastward acceleration of convergence and divergence zones are visible.

1. In the reference simulation the convergence zone quickly accelerates to stationary eastward propagation of about 2.5 m/s in the following 45-50 minutes, whereas it is substantially faster in ensemble member 3, with $\sim$ 4.3 m/s.

2. A weak acceleration of the divergence zone in the wake of the former zone occurs, most prominently in ENS-03.

3. Another stage of acceleration of this zone occurs at the end of the simulations (90-120 minutes, $x = 0$ to 30 km). However, this ocurs after the main analysis time and might be an effect of different reflections at the boundaries.

In addition to these main low level convergence features, convergence and divergence patterns associated with gravity waves are also visible in Figure 3. These comparatively weak waves lose amplitude in time. Apparent intermittent behavior in both figures for the western half of the domain is probably caused by the output interval of 5 minutes, approximately the apparent pulse frequency of these features.

A sudden displacement of the low level convergence zone happens after 0.6 hours (green oval, Figure 3) in ensemble member 3 (as opposed to the reference simulation), with a double divergence zone in its wake and an increase in amplitude of the convergence directly after. In the reference simulation this event happens in a smoother way: without a strong increase in amplitude of the convergence. On the contrary, the convergence zone also jumps by about a couple of km in ENS-03 and does not in the reference simulation. The jumpy displacement and amplitude increase of the convergence zone in ENS-03 is related to the initiation of secondary cells ahead of the squall line core (Section 3.1). The lower row panels of Figure 3 reveal a nearly stagnant and slightly diffuse patch of upper tropospheric divergence at $x \approx 0$ km, collocated with the squall line core. Propagation of this upper tropospheric divergence is clearly restricted to the second simulation hour for ensemble member 3. Furthermore, the consequences of developing convective cells (Section 3.1) are visible only after the first 15 minutes. Lastly, as in the lower troposphere, one can also see patterns associated with comparatively weak gravity waves propagating in the upper troposphere, originating from the initial and secondary convective cells, which leave the model domain after the first hour.

3.2.2 Secondary convective initiation and tracers

Tracers are a useful tool to identify the convective circulation of airmasses, as they provide quantitative information on the destination of specific inflow layers. Especially the circulation in the squall line and its individual cells can be described with this approach, comparable to a Lagrangian analysis. Of course the tracer analysis is restricted to the identification of transport from time of installation until given output time and to a coherent air mass. In the simulations the tracers PT1 and PT2 are initiated below altitudes of 2.5 km ahead of the squall line. Consequently, the mixing of air masses at low levels ahead of the squall line (and mainly the primary ascent) can be described with this information, whereas the effect of rearward entrainment from mid-levels and their diluting effect can only be analysed with much more difficulty. To evaluate the contrast between the simulation pair (Section 3.2.1) in more detail, passive tracers have been injected in the inflow of the two ensemble members (reference simulation and ENS-03). Tracer PT1 was implemented below 800 m between $x = 0$ and $x = 30$ km at $t = 0$ and PT2 was simultaneously initiated over the same horizontal region at all model levels where $1600 < z < 2400$ m. All concentrations were initially set to 0.001 kg/kg. These tracers are advected with the flow, with computations based on the advection scheme, but also the built-in subgrid turbulence of the LES. No sedimentation or other (microphysics-like) tendencies are contributing to their redistribution.

Analysing the differences of the passive tracer concentration between ENS-03 and the reference of PT2 after 30 and 35 minutes, peculiar patterns are found (Figure 4). The pattern consists of a surplus in PT2 after 30 minutes at the location of the black "X" in ENS-03 and a surplus about 1 km lower in the reference simulation, amongst others.

More precisely, a dipole structure in the PT2 surplus from $z = 4$ km to $z = 6$ km around $x = 0$ km at $t = 25$ minutes suggests

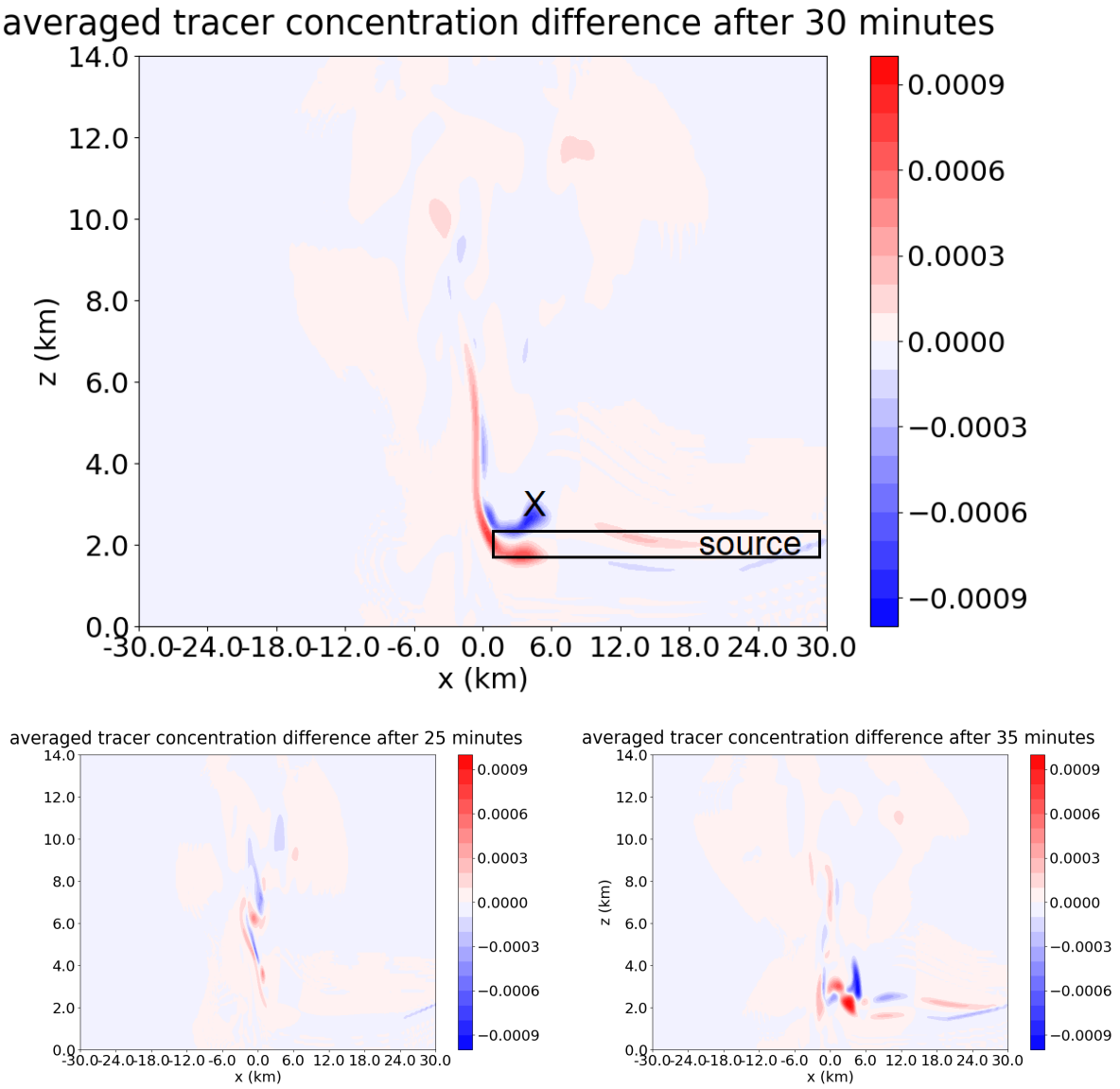

Figure 4. PT2 concentrations difference between reference and ENS-03 (reference minus ENS-03) after 30 min (top, a), 25 min (left bottom, b) and 35 min (right bottom, c). Red indicates a tracer surplus in reference simulation, blue in ENS-03. The black X (top, a) marks the gravity wave crest in which vertical displacement leads to triggering of a new line of convective cells in the squall line, as we will see later. Note that only half of the 120 km domain is shown.

a slight shift between the developing convective updrafts of the simulation pair in Figure 4. At $t = 30$ minutes the dipole has elongated vertically: the updraft core is shifted eastward by a few grid cells in ENS-03 compared to the reference. Furthermore the PT2 surplus at the location "X" in ENS-03 is very notable. At this location PT2 concentrations are much higher in ENS-03

than in the reference simulation at $z = 3$ km, a few km east of the x-axis. About a kilometer below PT2 concentrations are lower at the same time in ENS-03, at the lower flank of the source layer (Figure 4). A difference of opposite sign occurs at the top of (red; and below: blue) the PT2 source layer some 10 km to the east of X. After 35 minutes, the same signal has propagated eastward by some 5-7 km and the blue signal at location X has extended upward, but the red has not.

Consequently, PT2 transport is massively different between ensemble member 3 and the reference simulation, from t = 30 to t = 45 minutes: only 7.0% of the PT2 mass moves from its low level source layer to levels above 4 km height in these 15 minutes in the reference simulation, whereas 17.6% does in ensemble member 3. Furthermore, 11.7% (ENS-03) is flowing to the UT ($z > 6$ km) versus 6.0% (reference simulation). This implies a very large difference in convective tracer overturn and hence convective mass fluxes are significantly larger in ensemble member 3 than in the reference simulation.

Figure 5 displays the PT1 distribution after 55 and 75 minutes. Both PT1 and PT2 (not shown, similar patterns) indicate that

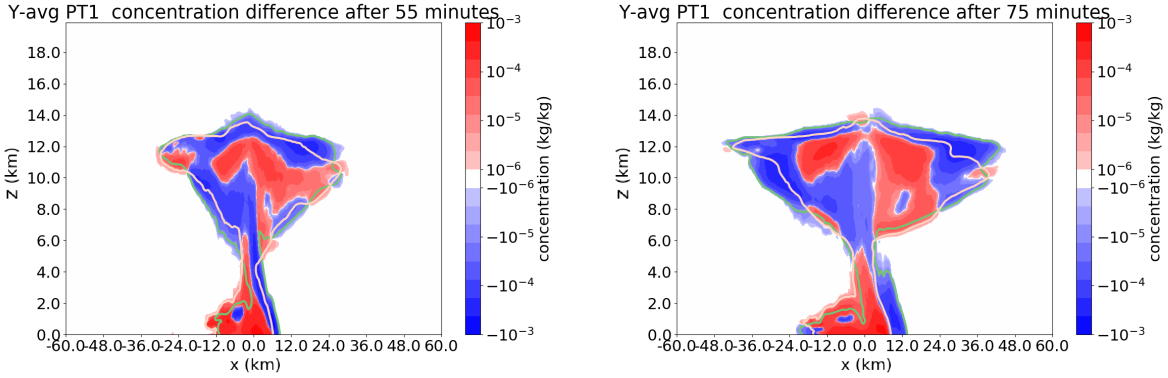

Figure 5. Difference in PT1 concentration between ENS-03 (blue: higher) and reference (red: higher), after 55 minutes (left) and 75 minutes (right) in colors. In addition, the $q_{PT2} = 1e-5$ kg/kg isoline is shown for both simulations (salmon**/bright pink** color: reference; green: ENS-03). Y-average is now taken over the limited subspace, consisting of 40 km$> y > -20$ km.

the top of the region with lower tropospheric tracers is lower in the reference simulation compared to the ENS-03. As the passive tracers are initiated at the location of source air for the convection, they reveal the source region of convected mass.

Two additional patterns are visible in the aforementioned figure: first, the near-surface eastern boundary of PT1 moves faster eastward (in blue, ENS-03) than in the reference simulation (red). Second, the tracer is laterally spread out further in ENS-03 (green contour, 5b) than in the reference simulation.

The three aforementioned patterns that PT1 shows (Figure 5) are a consequence of differential mass transport within the convection. Together with the patterns seen in PT2 earlier in this section, increased convective overturn in ENS-03 may lead to all of the three patterns. Extra mass overturn is consistent with the reflectivity patterns from Section 3.1.

The upper tropospheric divergence as visually demonstrated by the passive tracers is strongly increased in the ENS-03 (green) after 75 minutes compared to the reference. Upper tropospheric mass divergence averaged over a rectangular box volume

around the system up to 75 minutes differs by 38 % between the simulation pair, whereas the net latent heating left behind is only 24% higher in ENS-03 than in the reference simulation over the corresponding surface.

3.2.3 Vertical velocity at "X" and interpretation

Location "X" in Figure 4 has drawn specific attention, with a contrast between upward and downward displacements of PT2 in the reference simulation and ENS-03. These downward / upward displacements in the trough / crest are resembling gravity wave patterns, as it has been identified in the previous section. Furthermore, consequent differential vertical overturn of mass has been identified with tracer evolution directly afterwards.

The patterns identified in the former section therefore likely have a strong connection with vertical velocities at location "X", which could be affected by both variability in the gravity waves passing by first and then possibly by consequent variability in the potential for convective initation, corresponding to the lifting of air above its LFC. The mean w along the squall line at location X ($t = 30$ min) is +0.35 m/s in ENS-03 and -2.76 m/s in the reference, with along-line deviations of up to 1.5 m/s about the mean. Therefore, a large portion of X along the length of the squall line consists of favorable locations for initiation of convection in ENS-03 with $w > 0$, in contrast to the reference simulation, in which w is well below 0 at that position. Other ensemble members are at intermediate values between those two opposites, with a mean of -0.93 m/s. Given the spread of about 1.5 m/s in local w about the mean, most members contain some limited areas favorable for the secondary convective initiation.

3.3 Ensemble squall line variability

In this section the focus of the analysis is shifted towards the full ensemble, while variability in several important characteristics of the squall line has been detected between the two previously discussed members. Key aspects are the lag correlations of the cold pool edge with itself and the vertical velocity w at X (Figure 4). The relation of the latter with the meridionally averaged zonal cold pool relative flow (u) within the ensemble envelope is investigated. In the latter case, w of each ensemble member at location X acts as an independent variable. Additionally, other variables such as downdraft mass flux complement the holistic picture of the squall lines.

3.3.1 Location of the cold pool edge

The cold pool location and its time derivative, the propagation speed v_{cp}, are computed at each output step by taking the maximum of $\frac{\partial \rho}{\partial x}$ at the lowest model level. This computation over the zonal direction is done for each coordinate in the y-direction. The cold pool position and velocity are obtained by taking the average value of the resulting x over y and converting this to a corresponding grid cell index. This way, a cold pool edge is defined as a function of ensemble member and time. With this definition v_{cp} differs by a factor of 1.7 within the ensemble over the interval 30-75 minutes for the reference and ENS-03: 2.5 vs. 4.3 m/s. That simulation pair only differs by 47 m in initial interface height of the shear layer (< 2 %)! These simulations are on the outer ends of the ensemble distribution of cold pool velocity.

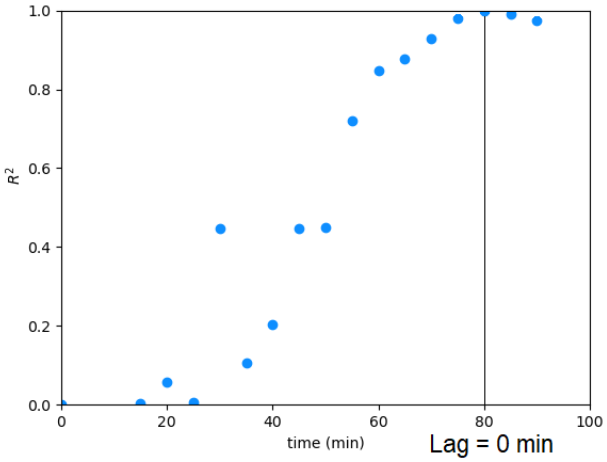

Figure 6. R^2 of lag correlations as a function of simulation time (indicated) for the cold pool position among 10 ensemble members, with the position at $t = 80$ minutes as reference correlation of 1. The points at $t = 5$ and 10 minutes have been ommited, as there is no variability in cold pool edge location among the ensemble members (yet).

The average displacement of the cold pool edge at the surface has been evaluated and lag correlated with its own location at $t = 80$ minutes, i.e. directly after the end time of the period before the squall line or its effects start leaving the domain in the zonal direction.

During the initial phase of the squall line development the ensemble spread of the cold pool edge location is very low (maximum of 1 grid cell), such that during that phase and given the small ensemble size, the results of the first 30 minutes are not very robust. As the ensemble spread in the cold pool location increases to 4 grid cells after 40 minutes and keeps on increasing linearly beyond, the uncertainty due to limited ensemble spread is substantially reduced and then eliminated. Consequently, beyond the 30 minute limit, the time evolution and lag correlation provides insight into the ensemble spread.

Figure 6 depicts an S-like shape of the lag correlation function. Roughly three stages can only be distinguished. First, there is a stage prior to establishment of the intra-ensemble variability in cold pool location (which will not be further discussed due to the low robustness mentioned above). Second, there is a stage where the intra-ensemble variability of cold pool location is establishing, corresponding with the growth stage of S-curve. In this stage the growth rate is maximised around 40-45 minutes. and the ensemble spread growth lasts from about 35-50 minutes. Third, there is a stage where the intra-ensemble variability is established, i.e. from about 50-55 minutes onward the cold pool location variability within the ensemble has been established and is maintained until 80 minutes (where $r = 1$) and beyond. In this stage, the cold pool locations relative to each other have been set and cold pools move jointly.

The ensemble variability structure is maintained. Both the standard deviation and the difference between maximum and minimum x of the cold pool edge increase nearly linearly beyond $t = 45$ minutes (not shown). This was also visually apparent for ENS-03 and the reference in Figure 3.

3.3.2 Ensemble sensitivity analysis

The ensemble sensitivity technique is applied to assess statistical patterns that exist in the squall line ensemble. Basically the ensemble sensitivity finds the regression line through the dimension of the ensemble members that describes the best fit between two variables x_1 and x_2, like in any analysis of covariance patterns (see also Hanley et al., 2013; Bednarczyk and Ancell, 2015). That means that perturbations or excursions in an x_2 with respect to an ensemble mean can be investigated in relation to those in variable x_1. Furthermore, the evolution of these perturbations of x_2 with time can be followed, as they are structured within the ensemble envelope. The information of conditional variability in x_2, conditional on x_1, is revealed and hence conditional coherent behavior of a spatial flow pattern related to x_1 later in time can be identified.

Bednarczyk and Ancell (2015) discusses some limitations of this analysis for a convective case, which apply specifically if the (spatial) extent of the independent variable is not exactly known and a proxy has to be used as in their case: deep convection was parameterized and precipitation or reflectivity related output had to be used instead. On the contrary, the spatial extent of a variable of interest is clearly delineated for this case in Section 3.2.2 and Figure 4 and it also directs at the independent variable, local w.

Since squall line variability is investigated here, the y-averaged variation in u in the x-z plane is of particular interest, especially within the squall line core. This core area with the updrafts, downdrafts and some inner portion of the anvil is the target variable of the ensemble sensitivity analysis.

The sensitivity of the squall line circulation to a precursor pattern in the velocity field is explored with the ensemble dataset. Therefore an ensemble sensitivity analysis targeted at u in relation to w at location X in Figure 4 is done. This w at X is averaged along the length of the squall line over five by five grid cells in the x-z plane: w_{loc}. A covariance analysis of w_{loc} is done with the y-averaged u in the x-z plane (i.e. u_{avg}) at any t in the simulation as covariant. Note that the ensemble sensitivity analysis is carried out in a cold pool edge relative framework: as this cold pool edge moves by up to 30 km during the simulations, correction for its displacement in x overlays various x-coordinates and thereby shrinks the available domain for the ensemble sensitivity analysis in the zonal direction by approximately 30 km from 120 to about 90 km.

The time evolution of correlation patterns in the squall line relative flow up to 25 minutes (during which statistically significant patterns are not identified) is presented in the supplementary material.

After 30 minutes, small undulations around the initial interface height z_i are visible in the obtained correlation patterns and a crest develops in the immediate wake of the cold pool edge ($x = -10$ km), while ahead of the cold pool edge a first signal of gravity wave activity is apparent ($x = 5$ to $x = 15$ km; Figure 7). Through w the latter wave signal is associated with the strong signal of convective initiation in ENS-03, which does apparently not occur in the reference simulation. In the following three time steps many more faster gravity wave signals propagate away from the source region. This source region of warm air upstream of the squall line would definitely pass the statistical significance test as a robust signal for $t = 30$ until $t = 60$ minutes. As the circulation is effectively almost 2D that is partly inherited by the fact that the circulation in the x-z plane contains both of the lagged variables from the statistical analysis: w at t = 30 minutes and u.

To investigate the second stage, the focus is shifted from the correlations of the ensemble sensitivity analysis to the second

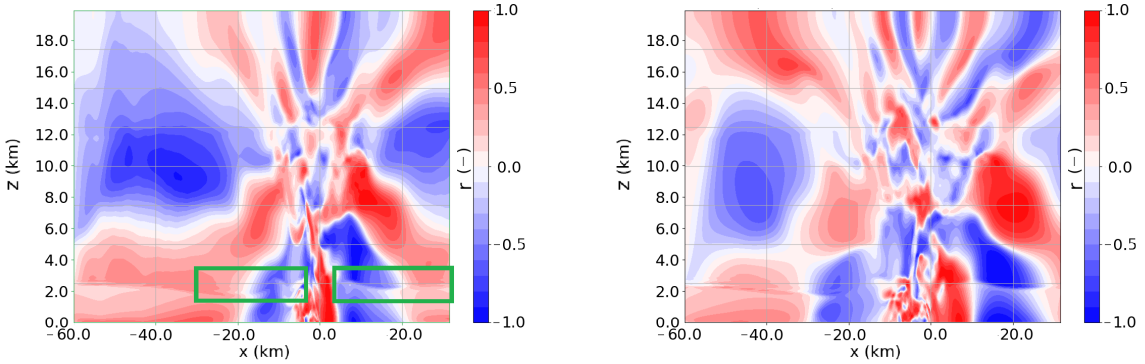

Figure 7. Correlation structure between w_{loc} and u_{avg} obtained from the ensemble sensitivity analysis. Left: $t = 30$ minutes, right: $t = 35$ minutes. On the left green rectangles are illustrating where "undulating wave signals" (see text) that resemble signals of gravity wave activity are located. One can see a gravity wave crest at $z_i \approx 2500$ m, propagating from $x = 4$ km to $x = 9$ km. With positive vertical velocity perturbations and inbound/converging u winds upon this crest, enhanced forcing for convective initiation ($x = 4$ km, $z = 3$ km, $t = 30$ minutes, X in Figure 4) is correlated with our target variable.

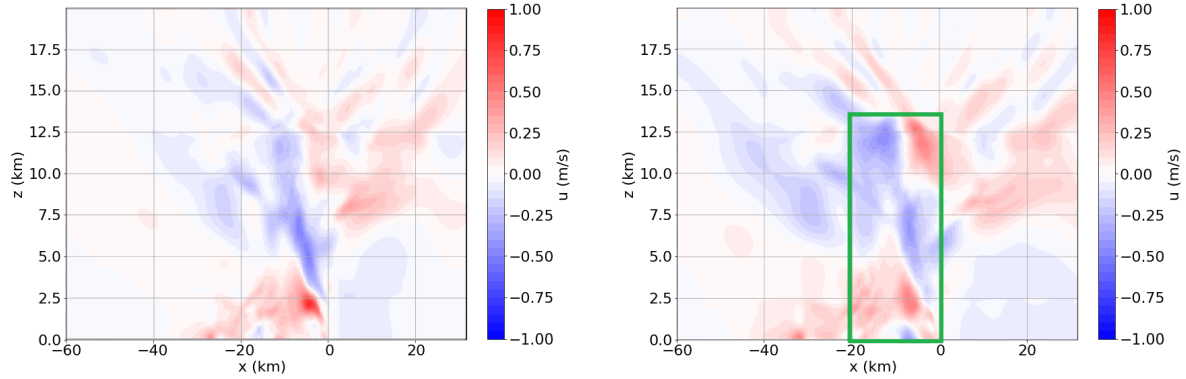

Figure 8. Domain with corresponding y-averaged u variance (relative to the cold pool edge) associated with w_{loc} after (left) $t = 50$ minutes and (right) $t = 55$ minutes. Among the main features are enhanced convergence in u around $z = 2.5$ km and $x = -4$ km, as well as enhanced divergence from $z = 7$ to $z = 13$ km. On the right, one can see extended divergence patterns (slightly) above $z = 13$ km, which is likely associated with an overshooting cloud top with divergent outflow in u. The central area of squall line circulation (see text) used for significance testing of the identified squall line circulation anomaly is marked with a green rectangle (only right figure).

covariant: the along-line average of relative u, depicted in Figure 8. The signals in u move from upright multi-wavenumber in the vertical, centered at the convective cells to one that is aligned with the tilted cold pool and another contribution that causes upper tropospheric divergence away from the convective cells in the anvil. Both of these signals of variability associated with

the squall line circulation occur after 40-50 minutes. Synchronously, the associated u variability also exceeds 1 m/s, maximizing at altitudes of 1.5 to 8 km (Figure 8a). The features of zonal flow still amplify in the higher regions of the troposphere and even up to the region of convective overshoot (Figure 8b), but also gradually propagate away from their source region in the following 30-40 minutes.

The signal of the this stage is statistically very robust: in the central 20 km of the squall line and at altitudes up to the tropopause a fractional area f of 0.56 passes the statistical significance test at $p = 0.05$ and $f = 0.35$ at $p = 0.0125$ (Figure 8b). This is more than an order of magnitude larger than random values (see also Wilks, 2016).

After 80 minutes, the u-variability associated with w_{loc} has weakened. Later some renewed variability occurs at $t = 90$ minutes (see supplement).

The circulation revealed by the ensemble sensitivity analysis demonstrates anomalous convergence of mass at $z = 2 - 3$ km, rearward of the cold pool edge (Figure 8). The convergence signal consists of enhanced easterly flow in the updraft region which gradually rises and moves upstream relative to the cold pool, due to the updraft tilt. The feature with easterly flow anomalies moves upward, extending initially ($t = 45$ minutes) from the surface to 8-9 km altitude. On its rearward side a westerly flow anomaly does roughly the same, but sticks to lower levels and dissipates earlier.

At the same time, another main feature in the sensitivity signal occurs in the upper troposphere: an enhanced upper tropospheric divergence at $t = 50$ minutes, which overshoots into the first 1-2 km of stratosphere at $t = 55$ minutes (Figure 8). This upper tropospheric pattern itself diverges in time and fades outward after about $t = 80$ minutes (see also supplementary material).

3.3.3 Downdraft variability and cloud tops

In this section the downdraft characteristics are discussed in more detail. Furthermore, the cloud tops are evaluated and then the statistical relations between the corresponding diagnostic variables and the two precursors (w_{loc} and system acceleration to v_{cp}) are quantified.

Downdraft detection

To compute the downdraft mass flux, area profiles of downdrafts and conditional vertical velocities in downdrafts, all grid cells with negative (positive for updraft detection) vertical velocities ($w < 0$ m/s) and a minimal total cloud hydrometeor density of 1e-4 kg/m^3 were selected. The downdraft area is given by the number of grid cells occupied in each layer. This computation method is inspired by and adjusted from Varble et al. (2020). Subsequently, gravity wave contributions from saturated parcels to downward motion are removed, by removing any grid cells where the total density ($\rho_{moist\_air} + \rho_{water}$) was lower than its horizontal average over that model layer. Downdraft parcels with negative vertical velocity but positive buoyancy would be manifestations of downward moving parcels with hydrometeor content that would not maintain their negative velocity, given their tendency to accelerate upward. Without the correction for gravity waves, downdrafts are highly overestimated in the near-tropopause region, where gravity wave activity is leading to substantial vertical transport of air with cloud hydrometeor content that is compensated by reverse motion in the vicinity (see also Pandya and Durran, 1996).

Any grid cell classified as downdraft is then used to calculate conditional mean of the vertical velocity w.

Cloud top detection

A cloud top definition has been selected using the simulated fraction of reflectivity beyond 15 dBz and an ice fraction above 1e-6 kg/kg as a cloud mask. The relative area covered by the cloud mask just after the convective overshoot (55-60 min, Figure 5) has been aggregated in time (60-90 minutes) and along the squall line as a function of z, as the anvil spreads out almost horizontally around equilibrium level. From several parameters, a fractional cloud cover of 0.1 in combination with a reflectivity of 15 dBz has been selected as most representative for the ensemble spread of cloud tops.

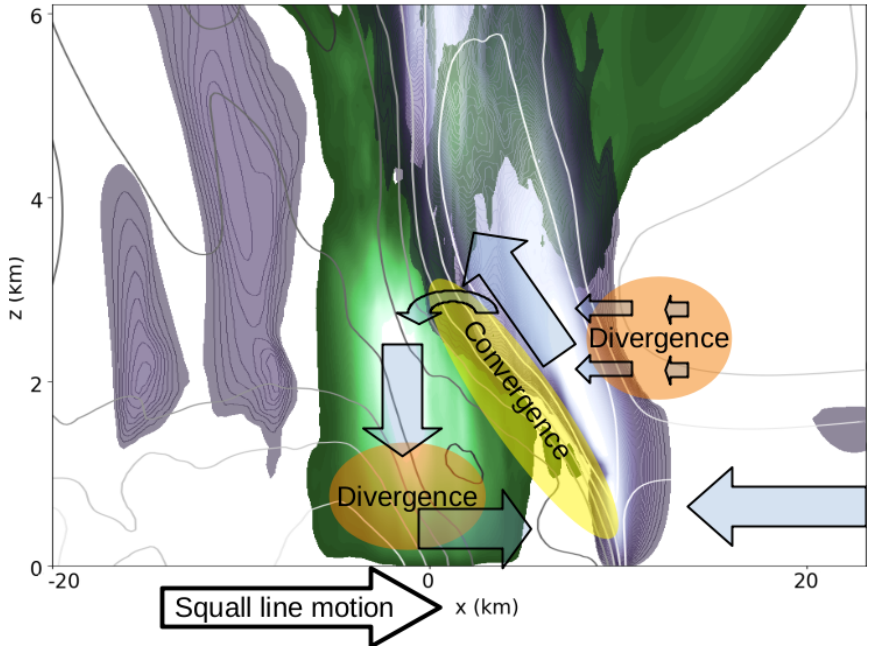

Figure 9. Schematic picture of the cold pool circulation in an x-z cross section: green coloring shows updraft mass fluxes, purple coloring shows downdraft mass fluxes. The white isolines indicate easterly flow (-9 m/s, every 3 m/s), while darkest grey ones indicate westerly flow (+6 m/s). One can identify convergence and divergence zones from these contours, which are conceptualized with yellow and orange ovals. The cold pool relative flow is given by light blue transparent arrows. Note that the classical pattern of a rear inflow jet (Houze, 2004, and references herein) is practically absent here and that the upper (roughly) half of the troposphere is omitted. The squall line propagation is given by the arrow at the bottom.

First, the y-averaged downdraft and updraft fluxes are displayed in an x-z cross section for one random ensemble member in Figure 9. This view depicts the numerical values for that simulation, but also includes a schematic overview of the circulation in the lower part of the squall line. It shows the updraft region on the forward flank of the squall line and a region of horizontal divergence (acceleration) at about 2 km ahead of the main ascent region. A substantial fraction of air masses in the upward branch continue their ascent into the upper troposphere. However, a certain fraction is also entrained in the downdraft region at or behind the cold pool edge. This edge is characterised by a region of convergence between the ascending and descending air masses. The downdraft, which is located mostly on top of the cold pool, causes low level divergence and causes propagation

of the squall line and cold pool edge towards the right. A rear-flank downdraft (or rear inflow jet) does not occur in this setup.

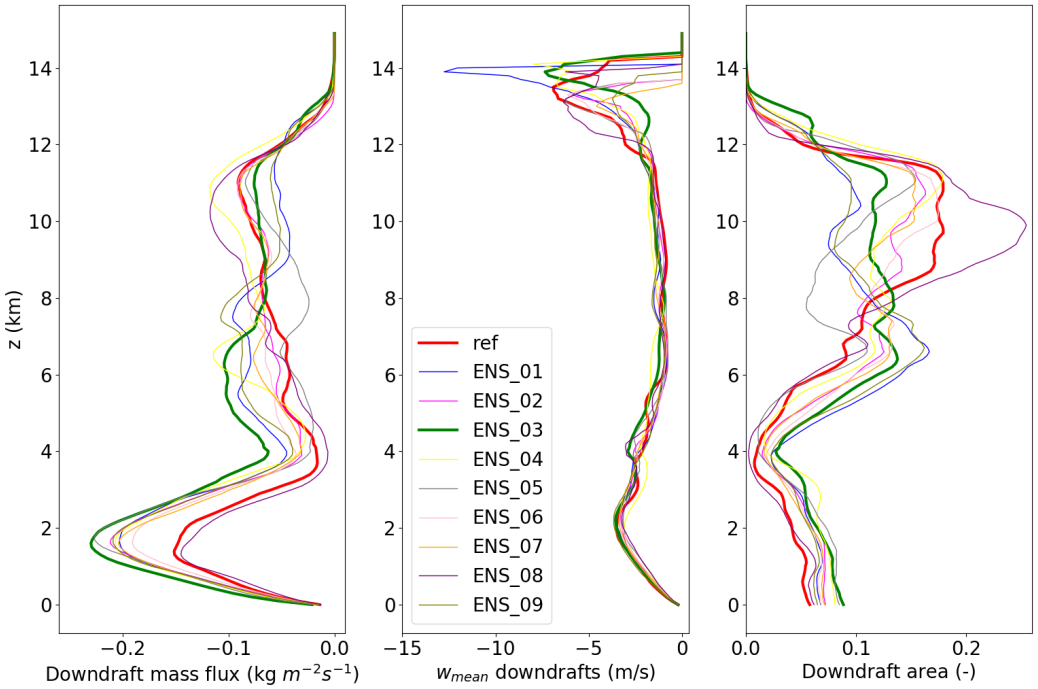

Figure 10. Instantaneous profile of squall line downdrafts at $t = 75$ minutes. Left: downdraft mass flux, center: mean conditional w, right: fractional area (reference and ENS-03: bold).

Most of the downdraft variability within the ensemble is achieved through downdraft area. This is depicted in Figure 10. However, this figure shows instantaneous values (at 75 minutes), in contrast to the time averaged values used for the statistical diagnostics. The left panel shows the downdraft mass fluxes, whereas the middle panel describes the conditional vertical velocity and the right most panel the area occupied by the downdrafts. While vertical maxima of the time averaged low level downdraft fluxes vary by up to 40% based on the ensemble envelope, the area of the downdrafts at the level of maximum fluxes explains about two third of this variability within the ensemble (even though the low level mean area in time varies by only half of that 40%). Additional contributions to the variability come mostly from the conditional mean of the downdraft velocity. In Section 3.3.2 a tilted convergence feature was identified, of which the intensity is amplified with increased w_{loc}. A part of the extra strong easterly flow in the updraft regions reaches this convergence zone and leaves the updraft on the upstream side for the convergence zone at the (upstream tilted) cold pool edge. Given the convergence with nearly stagnant air that moves approximately at v_{cp}, the downdraft fluxes below melting level are amplified at $z = 1 - 4$ km (Figure 10). The circulation

described in the earlier part of this paragraph could be thought of as a subcirculation within the squall line (Figure 9): a cold pool circulation. Given the convergence anomaly in Figure 8, positive covariance of the updraft and downdraft variability within the ensemble is found. That covariance may also imply a response of downdraft mass flux to the secondary convective initiation in Sections 3.1 and 3.2.

The statistical links between mean v_{cp}, w_{loc}, downdraft characteristics and other variables are presented in Table 1. Significant correlations between the downdraft properties and w_{loc} are found. The latter variable affects convective initiation, relates to overturned mass and in the end to the squall line relative flow perturbations. In Section 4 these and other connections will be analysed in more detail.

Table 1. Statistical relations between quantities of interest. $R^2 > 0.4$ is significant at $\alpha = 0.05$. Z_{max} in the table refers to the level where the low level downdraft flux maximizes ($z < 4$ km).

Precursor, Possible driver	**Effect, target**	**Time interval precursor (min)**	**Time interval target (min)**	$\mathbf{R^2}$
w_{loc}	v_{cp}	30	30-75	0.612
v_{cp}	Downdraft area at z_{max}	30-75	30-75	0.611
v_{cp}	Downdraft flux at z_{max}	30-75	30-75	0.799
v_{cp}	Precipitation flux	30-75	0-75	0.927
v_{cp}	Upper tropospheric divergence	30-75	0-75	0.595
v_{cp}	Cloud top height	30-75	60-90	0.559

3.4 Error growth in the squall line simulations

In this section the error growth is investigated, i.e. the increasing magnitude of the ensemble spread of the simulated squall lines. The ensemble spread of the horizontal winds with and without a correction for the cold pool propagation is analysed for that purpose. The latter approach allows for a comparison between a quasi-Eulerian and a feature relative perspective. This enables one to differentiate between a process based error growth and a feature location based increase of the ensemble spread. A limitation of this method is that only net growth of errors can be detected. Some processes can also reduce errors (e.g. diffusion) and so the method provides additional insight only when it finds growth in the error: a process leading to highly unbalanced tendencies dominates error tendencies. Negligible initial errors typically lead to error growth to a certain climatological envelope on long time scales and infinite time limit, which makes the error growth analysis a useful tool here.

Similar to the ensemble sensitivity, diagnosis of error growth is targeted at variability in squall line relative flow here and therefore applied to the u winds in the x-z plane. The zonal wind is averaged in the y-direction, wherever the cold pool relative framework is used. The zonal wind approach is differs from a more complete energy metric (Selz, 2019; Zhang et al., 2007; Zhang, 2005), which includes u^2, v^2 and may sometimes also include T. The growth of ensemble error as a measure of ensemble variability is mapped by the difference in winds between ensemble pairs. The simulations that such a pair consists of are usually assumed to fulfil a perfect "error" assumption, analogous to a perfect model assumption (see Selz, 2019): note, that

only the error needs to fulfill this assumption and not the full model itself. With this, growth rates of error energy (difference kinetic and/or difference total energy, Zhang (2005)) can be compared with expected behavior.

Figure 11 shows the error growth curves. The v-component is not included, but it is typically at least comparatively much smaller than u in the simulated scenario, and therefore, u reveals the dominant error patterns. Nevertheless, the part of the domain downstream of the squall line is not fully included. The cold pool relative frame work leads to a direct comparison of u winds at x-coordinates that are a function of the ensemble member. As the series of x-coordinates that can be covered depends on the cold pool position in each ensemble member, about a quarter of the domain is lost by taking the cold pool relative view. A first major stage of growth occurs between $t = 20$ and $t = 30$ minutes in both the 'absolute' and 'relative' $(\Delta u)^2$. This stage of the error growth is likely driven by decorrelation of the gravity wave phase and amplitude, and to some extent by differences in the convective initiation, as also analysed in Section 3.2.2. This early stage does not cause much variation between the corrected and uncorrected error curves, because the cold pool edge has hardly moved in the early stage. However, some variation can occur due to the inclusion of the full domain for the grid point based comparison versus only three quarter of it for the v_{cp} corrected and y-averaged curves.

Another second major stage of error growth occurs from 40 or 45 minutes to 60-65 minutes. The variability in the squall line flow (Figure 8) strongly develops during this stage. In this stage the slope between the corrected and uncorrected curves is systematically different, with much larger slopes for the grid point based curves. This means that a substantial portion of variability in squall line relative circulation can be explained and is probably induced by variability in the cold pool propagation speed (v_{cp}). However, even the relative framework is applied, some of the ensemble members still demonstrate strong error growth, whereas others do hardly show error growth compared to the reference simulation. The impact of non-linearities and feedbacks that affect error growth as well are obviously present, but during this stage non-linearities definitely do not dominate over v_{cp} effects. Roughly estimated, after about 60 minutes of simulation time about a third to half of the error is related to differential cold pool propagation and another third to half of the total errors was pre-existing after 30 minutes. Even though the latter two contributions are not fully independent, this means that non-linearities must be of a magnitude that is somewhat comparable to the two.

Moreover, both the corrected and uncorrected error curves seem to grow linearly in the second stage. In combination with the relatively constant v_{cp} values in each simulation (Section 3.3.1), it implies that the cold pool acceleration linearly explains a substantial proportion of variability in the squall line circulation and possibly even the majority of the errors.

Another notable feature between the two identified main stages of error growth in the error growth curves is the relatively low slope of the v_{cp}-corrected curves from 25-30 to 40-45 minutes. This can be explained by a combination of regions of error growth and other regions where errors decay. Error growth mostly occurs in the regions of secondary convective initiation. The spatial distributions of difference winds strongly suggest that the decay of errors mostly happens at locations of difference wind maxima after 25 minutes in the upper tropospheric region with cell cores, around $x = 0$ km (not shown). That implies the relatively flat curve after 30-40 minutes is not inconsistent with local error growth due to secondary convective initiation.

After the first 60-65 minutes (Figure 11), the cold pool corrected curves do not seem to grow anymore, but errors remain rather stable. Moreover the ensemble members with large $(\Delta u)^2$ do seem to have a stable v_{cp}-corrected $(\Delta u)^2$ in the second hour.

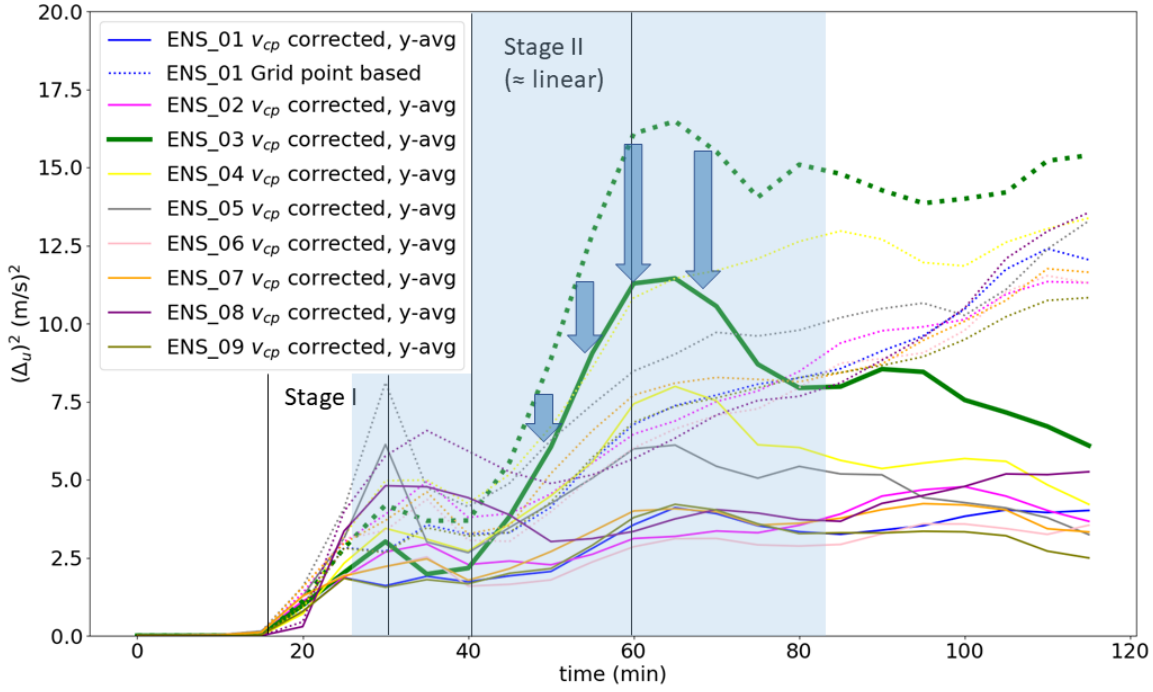

Figure 11. Error growth as measured by the ensemble variance in u, where each other member paired with the reference simulation. Both cold pool edge location corrected curves (solid lines) and grid point based comparisons (dotted) are displayed. Growth stages discussed in the text are also annotated in the Figure (see text) and the key interval discussed in the analysis is highlighted by blue shading.

Summarising this section, two main stages of error growth have been identified, with no growth in between those two stages of accelerated error growth. The second of two stages reveals interesting near-linear relations with the cold pool edge propagation.

4 Synthesis and Discussion

4.1 Evolution of ensemble spread

4.1.1 First amplification of ensemble spread: secondary convective initiation

The ensemble sensitivity analysis has demonstrated statistical correspondence between w_{loc} and flow patterns in the x-z plane elsewhere in time and space. In the section on the passive tracers (Sections 3.2.2) it has been shown that the updraft position after about 25 minutes of simulation time is already associated with differential w_{loc}. The time evolution and spatial patterns

of a through (resp. crest) in both the tracer distribution and the ensemble sensitivity confirm that the propagation of differences in both amplitude and phase of a gravity waves is initiating a vertical velocity difference. This vertical velocity contrast is able to trigger extension of the convective cells a few km to the east after about 30-35 minutes - the secondary convective initiation in part of the ensemble and most notably in ENS-03. The secondary initiation directly impacts convective overturning: subsequently, ENS-03 and the reference simulation reveal a large difference in upward tracer flux of PT2 to levels above 4 and 6 km associated with the deep convection.

4.1.2 Second phase in the evolution: cold pool acceleration

After the secondary phase of initiation happens (30-35 minutes), the upward mass flux within the convection is not only increased. The cold pool is also accelerated (around 35-45 minutes) to a speed that is later on maintained, as was suggested by the lag correlation function of the cold pool edge location (Section 3.3.1). The cold pool velocity is higher for ENS-03 with more convective overturn. One could anticipate that more convective overturn (updrafts) also leads to increased downdraft intensities. As the strengthening of updrafts is caused by eastward extension of the updrafts, one could also expect a consequent increase in downdraft area. Statistics reveal significant intra-ensemble correlation between the maximum downdraft flux as well as downdraft area at the level of maximum downdraft flux (30-75 min) with cold pool velocity (30-75 min).

Further support of the importance of cold pool acceleration in this stage is provided by the error growth curves in Section 3.4. This error growth curve starts to grow strongly in the gravity wave de-correlation and first convective initiation phase (20 minutes) and continues to do so during the first part of the secondary initiation phase (30-35 minutes). Directly after that instance, the error growth stagnates for a short period (around 35-40 minutes). Curves where a correction is made for cold pool velocity clearly demonstrate less error growth in the subsequent phase than the uncorrected curves. It implies some presence of feedback and interactions other than direct effects of cold pool propagation spread as source of ensemble variation, but an important mode of variability contained within the ensemble is certainly associated with the contrasts in the cold pool velocity. The linear contribution of cold pool propagation is about as important to the errors as other non-linear feedback mechanisms in the second stage of error growth (40-60 minutes).

The secondary phase of initiation (30-35 minutes) and subsequent cold pool acceleration (35-50 minutes) is the most important event for the ensemble spread.

4.1.3 Common mode of variability and possible common driver

The common driver for a substantial fraction of the squall line variability, including the cold pool acceleration to a stable value of v_{cp} is the gravity wave development originating from the first convective initiation. It influences the secondary convective initiation and the cold pool propagation. In the example of strong secondary triggering (ENS-03), convergence originating from the gravity wave crest compensates for upward motion. This convergence pattern below the gravity wave crest implies that the cold air on the rear flank is likely accelerated a bit more eastward relative to the reference member, in which no secondary initiation occurs. This additional eastward motion leads to more mass reaching the region of initial downdrafts, accelerating the cold pool circulation. This is also consistent with Hovmöller diagrams of the cold pool in ENS-03 and the reference

simulation, because immediately after the secondary initiation the cold pool in ENS-03 occupied a larger area (supplement Figure S5). In addition, this is supported by the tracer evolution after 30-35 minutes. The statistical links between w_{loc}, v_{cp} and downdraft area and mass flux are confirmed by Table 1 and the convergence patterns in the ensemble analysis.

Overall, this common mode of variability increases the vertical overturning in both upward and downward mass fluxes, by increasing the intensity of the cells. This in turn affects the downdraft strength and leads to precipitation differences. Moreover, the mode of variability probably induces some of the variability in strength of convective overshooting into the stratosphere after about 60 minutes and the strength of mean upper tropospheric divergence (see Table 1). Therefore, a common driver of squall line variability exists, of which we have found w_{loc} as an early manifestation.

This w_{loc} is the earliest identified manifestation of the common mode of variability. It may be present before this manifestation, hidden in the gravity wave variability. The mode of variability lives on for the next 45-60 minutes.

4.1.4 Approach of intrinsic limit?

The tiny initial difference (less than 2% in terms of shear layer depth) implies that the mode of variability is very sensitive to initial conditions. Given that the total variability in initial shear layer depth was 5%, it can be argued in line with Melhauser and Zhang (2012) (in particular based on the illustration in their Figure 18) that there can occasionally be an intrinsic limit of predictability on time scales of about an hour. A pattern very closely matching such behavior is exposed by the presented simulations and analysis, after doing a perfect error assumption (see Selz, 2019).

The non-linear behavior in the evolution from initial conditions to $t = 30$ minutes indicates the potential for an intrinsic limit of predictability. The 'random' realisation of gravity wave amplitude and phase after ~ 30 minutes leads to random excitation of the identified mode of variability: Figure 4 suggests a possibility that amplitude and phase of gravity waves could possibly be directly responsible for w_{loc}. This non-linearity in the evolution between $t = 0$ and $t = 30$ minutes directly implies that characteristics of the initial conditions cannot be monotonically linked with the conditions afterwards, including those during the secondary phase of initiation. These resulting conditions also include the flow anomalies (or perturbations) associated with the squall line as found in Section 3.3.2. Initial condition perturbations are non-linearly linked with much of the squall line variability that occurs after 30-85 minutes. Therefore the illustration of Figure 18 in Melhauser and Zhang (2012) fits to the here presented findings and it can be argued that intrinsic sensitivity is a key implication.

4.1.5 Squall line flow perturbations

The flow perturbations in the squall line were very likely affected by w_{loc} and so by the common mode of variability that we suggest. It builds up after about 40-45 minutes of simulation time and relation with w_{loc} peaked after 55-60 minutes. The anomalous flow pattern in the squall line, as shown in Figure 8, resembles to some extent that of an enhanced circulation of the jump updraft, downdraft and overturning updraft as in Moncrieff (1992). The figure suggests that the mode of variability identified in this study is partly explained by intensification of this 2D circulation after 45-85 minutes of simulation time.

During the second hour of simulations the traces of the identified mode of variability seem to disappear gradually. The gradual dissipation of the initial mode of variability was identified by the ensemble sensitivity analysis between about 70 and 85

minutes, with a new structure of u variability appearing, which is partially opposing the earlier circulation signal in terms of zonal flow. In combination with the flattening error curve in Figure 11 during the second hour this might suggest a sign of saturation, where (Δu) reaches about 4 m/s. That value is a significant fraction of the actual u, but roughly only halfway of the absolute value.

There is a possibility that the identified common mode of variability covaries with a subhourly time scale imposed on the squall line by cyclic behavior during its growth as in McAnelly et al. (1997) and Adams-Selin (2020a).

4.2 Discussion

The squall lines in this study, which are initiated with a cold pool structure, start getting mature only later on in the 120 minute simulation. Furthermore, the simulations are restricted to a relatively small domain. Parts of mature and the dissipation state of the system are excluded. Still, this study is able to depict that small errors in the initiation phase lead to a systematic variability of the convective system. A different set-up (e.g. larger domain, different boundary conditions and an extended simulation time) could provide some more insights into the development of ensemble spread during the mature phase of the system. Nevertheless, this study identifies a highly relevant window for squall line error growth in the first 80 minutes of the development, in which systematic variability in the squall line relative flow has fully developed and also decays.

The setting in this study is very similar to that in Adams-Selin (2020a, b). The main difference in the environmental conditions is that this study has a reduced depth of the shear layer to about half of their environment. Furthermore, the domain and geometry was different: squall lines in this study behave as "infinite" length squall lines. There is also similarity in the evolution in the sense that a discrete propagation event on small length scales is diagnosed, or at least a new cell growing ahead of our squall line. In our simulation this occurs a lot earlier: already after 30 minutes and just after the first phase of convective initiation. Furthermore the event occurs only a couple of km ahead of the squall line, as opposed to the clearer separation in Adams-Selin (2020a, b); Fovell et al. (2006). Even though one could wonder whether this study is an actual discrete propagation event or just growth ahead of the squall line, Figure 4 suggests it starts as a discrete propagation event. Quite soon this event is absorbed by the squall line itself. Certainly, the discrete propagation event detected in Fovell et al. (2006) could not happen as closely ahead of the squall line as in the presented simulation, as the resolution was lower then and small updrafts are often at the minimum size possible in the simulation. However, the presented results demonstrate that distinct convective initiation only about 3 km ahead of a squall line can easily be resolved at 200m resolution. With a resolution below 100m one could assume that events like discrete propagation could be simulated in LES when they happen at length scales of 500-1000m. This would require a higher output frequency, as in Adams-Selin (2020a, b).

A degree of similarity is also shared with Weyn and Durran (2017), even though these authors use warm bubbles and slightly different temperature, moisture and wind profiles with deeper shear of varying magnitude. In spite of their analysis mostly carried out in spectral space, their error growth curves of mesoscale convective systems can be compared to ours. The main difference is first of all that the simulations in this study take place in a smaller domain and at higher resolution for a shorter integration time. They run their simulations up to six hours, which leads to error saturation ($> 75\%$) after 4.2-6.0 hours. In the simulations presented here, error saturation is not reached. Moreover, the occurrence of some humps with stages of no

error growth in the error curves is shared with their Figure 8, but theirs appear relatively small in magnitude. However, for an assessment of error saturation their study provides a much more suitable approach - the simulations here have not been integrated far enough and the metrics are not so suitable for that assessment. However, error saturation is beyond the scope of this study.

Even though Weyn and Durran (2017) approach squall line predictability from a different perspective, this study provides an additional foundation on how squall line predictability may be extended very slightly only (on the order of an hour) when initial conditions are very accurately known: initial conditions are non-linearly linked to the secondary phase of convective initiation and the secondary phase of initiation is highly sensitive to these initial conditions. On the other hand, the findings also suggest that some of the information on convective initiation can be stored as linear signals in the squall line relative circulation that live for time scales on the order of one hour, while feedback effects are of secondary importance. That finding once more confirms the known ideas of shorter and shorter saturation time scales for smaller and smaller scales (Lorenz, 1969; Durran and Gingrich, 2014).

The ensemble in this study starts with highly but not fully 2D initial conditions, as part of a wide spectrum from highly simplified squall line studies (see Houze, 2004, for references) to more recent simulations of real cases coupled to the large scales (e.g. Melhauser and Zhang, 2012). The applied initial conditions are apart from the depth of the shear layer practically the same as those in Adams-Selin (2020a). The high degree of 2D makes the variety of diagnostics applied here much more affordable to assess, which is particularly beneficial in error growth studies. Even if not completely representative for many squall lines in the real atmosphere, convergent rolls often organise convection and occur along real squall lines. Insights in error growth provided here and in processes responsible for error growth are likely largely applicable along sections of real squall lines, especially those closely relating to findings of Melhauser and Zhang (2012). The idealisation only emphasizes signals, which is of benefit to the analyses.

The robustness of statistical results may appear somewhat questionable at the very first glance even after statistical tests, given that only two simulations are compared in Section 3.2 and given the ensemble size of just $n = 10$. Nonetheless, the very high correlations in Section 3.3.2 easily survive any significance tests with a null hypothesis that correlations found are random, consequently verifying the robustness of the signal. Significance measures with which the ensemble sensitivity analysis survives the tests implied very high confidence in the statistical robustness of the signal. In other words, larger ensembles would reveal the same signal as the 10 member ensemble, given the outcome of the statistical test. As confirmed by the uncorrected error growth curves, the signal of the main mode of variability is demonstrated to be well established and well separable from noise and non-linear contributions. These non-linear components consist of the feedbacks that do occur to a limited extent. The ensemble sensitivity analysis reveals the main mode of squall line variability, which is strongly related to the secondary phase of convective initiation with high confidence.

The relations found in this study indicate that cold pool acceleration after about 30 minutes of simulation time is very likely explained by the main mode of variability and hence by variability in gravity wave propagation. One could argue that the depth of heating profile immediately before cold pool acceleration can affect the vertical wavelength and propagation speed of gravity waves of a certain wavenumber, in agreement with findings by Pandya and Durran (1996). A heating profile depth differing by

1 km would provide a variability in cold pool propagation of about 8-10% for a 12 km deep troposphere and explain an 8-10% difference in cold pool propagation speed. If a wave has a vertical wavenumber of $n = \frac{5}{2}$ over twice the depth of the troposphere or a vertical wavelength of about 10 km, it will propagate at about 17 m/s. That wavelength is equal to wavenumber one in the layer between the surface cold pool and the tropopause. Against easterly near-surface winds that are on the order of 12-14 m/s these gravity waves would propagate eastward relative to this near-surface flow at low speeds of 3-4 m/s: the density current could surf on this wave. The 1.7 m/s difference in propagation velocity between ENS-03 and reference is consistent with this. Inspection of the precursor condensation rates after 25 minutes (before the gravity wave leads to secondary initiation) suggests a deviation in heating profile depth of at least 500 m between ENS-03 and the reference simulation, probably close to 1km. Furthermore, cloud top detections between the two deviate by 800m after 60-90 minutes of simulation time. In other words, there is support for this argument. The arguments are comparable to Grant et al. (2018) and references herein and Stechmann and Majda (2009). Whether the gravity wave propagation actually leads to differential cold pool acceleration is beyond the scope of our study. It would require a detailed minute by minute analysis for the 20-30 minutes interval (with sub-minute output frequencies), including a computation and analysis of additional quantities such as the Scorer parameter.

5 Conclusion

This study compares an ensemble of idealised squall line simulations with nearly identical initial conditions. It demonstrates that some degree of linearity in the error growth of the convective event is maintained throughout the second half hour of the simulation, during which the squall line grows towards the mature stage. A secondary phase of convective initiation after ~ 30 minutes has been identified as crucial for the evolution of the ensemble spread. The mode of variability associated with this secondary phase of initiation has been identified as shifts in phase and amplitude of gravity waves triggered by the developing squall line itself, originating from the very small initial disturbances. It is first revealed by the upward motion a few km ahead of the squall line after 30 minutes. Leading to contrasts in secondary initiation of convection, the effect of this mode of variability on the squall line through upward tracer and mass transport, downward mass transport, cloud top height and variability in squall line circulation can be followed. Its effect is most clearly present after 55-60 minutes of simulation time. After almost an hour of existence this mode of variability gradually disappears (70-85 minutes).

It is concluded, that in good agreement with Melhauser and Zhang (2012); Hanley et al. (2013) convective initiation sensitively depends on environmental conditions in the presented ensemble of idealized simulations. The chain of interactions has been documented in much detail: following the crucial secondary initiation phase, a cold pool acceleration is coupled to the intensity at which mass is moved by updrafts and downdrafts. On the other hand, once established (35-45 minutes), the cold pool velocity v_{cp} is maintained well throughout the next 30-45 minutes, as shown by Section 3.3.1. Variation in v_{cp} explains much of the subsequent variance in cold pool perpendicular flow (u) and therefore a substantial fraction of it is explained by the mode of variability identified in this study. It is shown by Eulerian and feature-centered perspectives, that both the cold pool propagation itself and non-linear feedback mechanisms play a substantial role in the idealised squall line ensemble after 45-60 minutes. Consequently, two stages of error growth are identified:

- De-correlating gravity wave patterns originating from the initial triggering of convection.
- A stage associated with the main mode of squall line variability, which to a substantial degree depends linearly on v_{cp} and the secondary phase of convective initiation.

Noteworthy, initial condition uncertainties lose their structure and less than 2% variation in initial top height of the shear layer z_i can result in convective intensities and overturned mass at opposite ends of an ensemble with 5% initial variation in that z_i. An explanation for the loss of structure is likely that non-linear developments in the triggered gravity wave signals (phase, amplitude, stage after 20-30 minutes) are a precursor to the phase of secondary initiation. This loss of the initial structure can lead to very different developments of the squall line in the mature stage and the ensemble can chaotically diverge towards a wider envelope, where information about earlier states is lost. Loss of uncertainty structure within a narrow ensemble with squall line simulations is in good agreement with the picture that Melhauser and Zhang (2012) draw for intrinsic and practical predictability at the end of their study. Comparably to their findings, it can be concluded from this study that a very small subspace in initial conditions can provide the same ensemble spread as a much wider subspace: an intrinsic limit of predictability may be present.

Code availability. A readme file for the amended namelist file and main output data of simulations are available at https://tinyurl.com/groot-tost-22 (Groot, 2022)

Author contributions. EG designed, conducted and composed the content of this study as part of his PhD project, with contributions from and under the supervision of HT.

Competing interests. HT is also a co-editor of this journal. However, this does not represent a competing interest for this publication; there are no further competing interests.

Acknowledgements. The research leading to these results has been done within the subproject 'A1 - Multiscale analysis of the evolution of forecast uncertainty' of the Transregional Collaborative Research Center SFB / TRR 165 'Waves to Weather' funded by the German Research Foundation (DFG). HT acknowledges additional funding from the Carl-Zeiss foundation.

Parts of this research were conducted using the supercomputer MOGON 2 and advisory services offered by Johannes Gutenberg-University Mainz (hpc.uni-mainz.de), which is a member of the AHRP (Alliance for High Performance Computing in Rhineland-Palatinate, www.ahrp.info) and the Gauss Alliance e.V. The authors gratefully acknowledge the computing time granted on the supercomputer MOGON 2 at Johannes Gutenberg-University Mainz (hpc.uni-mainz.de).

The authors would like to thank Michael Riemer, Mirjam Hirt, Annette Miltenberger, Peter Spichtinger, Christopher Polster, Amelie Mayer and Sören Schmidt for their contributions through constructive feedback and/or suggestions to improve (sections of) the manuscript, methods and/or improving the presentation in some figures.

References

Adams-Selin, R. D.: Impact of Convectively Generated Low-Frequency Gravity Waves on Evolution of Mesoscale Convective Systems, Journal of the Atmospheric Sciences, 77, 3441 – 3460, https://doi.org/10.1175/JAS-D-19-0250.1, https://journals.ametsoc.org/view/journals/atsc/77/10/jasD190250.xml, 2020a.

Adams-Selin, R. D.: Sensitivity of MCS Low-Frequency Gravity Waves to Microphysical Variations, Journal of the Atmospheric Sciences, 77, 3461 – 3477, https://doi.org/10.1175/JAS-D-19-0347.1, https://journals.ametsoc.org/view/journals/atsc/77/10/jasD190347.xml, 2020b.

Adams-Selin, R. D. and Johnson, R. H.: Examination of Gravity Waves Associated with the 13 March 2003 Bow Echo, Monthly Weather Review, 141, 3735 – 3756, https://doi.org/10.1175/MWR-D-12-00343.1, https://journals.ametsoc.org/view/journals/mwre/141/11/mwr-d-12-00343.1.xml, 2013.

Bednarczyk, C. N. and Ancell, B. C.: Ensemble Sensitivity Analysis Applied to a Southern Plains Convective Event, Monthly Weather Review, 143, 230 – 249, https://doi.org/10.1175/MWR-D-13-00321.1, https://journals.ametsoc.org/view/journals/mwre/143/1/mwr-d-13-00321.1.xml, 2015.

Bierdel, L., Selz, T., and Craig, G.: Theoretical aspects of upscale error growth through the mesoscales: an analytical model, Quarterly Journal of the Royal Meteorological Society, 143, 3048–3059, https://doi.org/10.1002/qj.3160, https://doi.org/10.1002/qj.3160, 2017.

Bretherton, C. S. and Smolarkiewicz, P. K.: Gravity Waves, Compensating Subsidence and Detrainment around Cumulus Clouds, Journal of Atmospheric Sciences, 46, 740 – 759, https://doi.org/10.1175/1520-0469(1989)046<0740:GWCSAD>2.0.CO;2, https://journals.ametsoc.org/view/journals/atsc/46/6/1520-0469_1989_046_0740_gwcsad_2_0_co_2.xml, 1989.

Bryan, G.: Cloud Model 1. Version 19.8/cm1r19.8, retrieved/downloaded from: *https://www2.mmm.ucar.edu/people/bryan/cm1/*, 2019.

Bryan, G. H., Wyngaard, J. C., and Fritsch, M. J.: Resolution Requirements for the Simulation of Deep Moist Convection, Monthly Weather Review, 131, 2394–2416, 2003.

Coniglio, M. C., Stensrud, D. J., and Wicker, L. J.: Effects of upper-level shear on the structure and maintenance of strong quasi-linear mesoscale convective systems, Journal of the Atmospheric Sciences, 63, 1231–1252, https://doi.org/10.1175/jas3681.1, 2006.

Deardorff, J. W.: Stratocumulus-capped mixed layers derived from a three-dimensional model, Boundary-Layer Meteorology, 18, 495–527, https://doi.org/10.1007/bf00119502, 1980.

Durran, D. R. and Gingrich, M.: Atmospheric Predictability: Why Butterflies Are Not of Practical Importance, Journal of the Atmospheric Sciences, 71, 2476 – 2488, https://doi.org/10.1175/JAS-D-14-0007.1, https://journals.ametsoc.org/view/journals/atsc/71/7/jas-d-14-0007.1.xml, 2014.

Fovell, R. G., Mullendore, G. L., and Kim, S.-H.: Discrete Propagation in Numerically Simulated Nocturnal Squall Lines, Monthly Weather Review, 134, 3735 – 3752, https://doi.org/10.1175/MWR3268.1, https://journals.ametsoc.org/view/journals/mwre/134/12/mwr3268.1.xml, 2006.

Grant, L. D., Lane, T. P., and van den Heever, S. C.: The role of cold pools in tropical oceanic convective systems, Journal of the atmopsheric sciences, 75, 2615–2634, https://doi.org/10.1175/jas-d-17-0352.1, 2018.

Groot, E.: Output data and namelist - README file 'Evolution of squall line variability and error growth in an ensemble of LES' [dataset], https://doi.org/10.5281/zenodo.6619313, https://irods-web.zdv.uni-mainz.de/irods-rest/rest/fileContents/zdv/project/m2_jgu-w2w/w2w-a1/EG_HT_2022_squall_line_var/README.txt?ticket=tfKfvC272uyo1WC, also available at https://doi.org/10.5281/zenodo.6619313 and https://tinyurl.com/groot-tost-22, 2022.

Hanley, K. E., Kirshbaum, D. J., Roberts, N. M., and Leoncini, G.: Sensitivities of a Squall Line over Central Europe in a Convective-Scale Ensemble, Monthly Weather Review, 141, 112 – 133, https://doi.org/10.1175/MWR-D-12-00013.1, https://journals.ametsoc.org/view/journals/mwre/141/1/mwr-d-12-00013.1.xml, 2013.

Houze, R. A.: Mesoscale convective systems, Reviews of Geophysics, 42, https://doi.org/10.1029/2004rg000150, 2004.

Houze, R. A.: 100 Years of Research on Mesoscale Convective Systems, Meteorological Monographs, 59, 17.1 – 17.54, https://doi.org/10.1175/AMSMONOGRAPHS-D-18-0001.1, https://journals.ametsoc.org/view/journals/amsm/59/1/amsmonographs-d-18-0001.1.xml, 2018.

Lane, T. P. and Reeder, M. J.: Convectively Generated Gravity Waves and Their Effect on the Cloud Environment, Journal of the Atmospheric Sciences, 58, 2427 – 2440, https://doi.org/10.1175/1520-0469(2001)058<2427:CGGWAT>2.0.CO;2, https://journals.ametsoc.org/view/journals/atsc/58/16/1520-0469_2001_058_2427_cggwat_2.0.co_2.xml, 2001.

Lane, T. P. and Zhang, F.: Coupling between gravity waves and tropical convection at Mesoscales, Journal Of The Atmospheric Sciences, https://doi.org/10.1175/2011JAS3577.1, 2011.

Lebo, Z. J. and Morrison, H.: Effects of Horizontal and Vertical Grid Spacing on Mixing in Simulated Squall Lines and Implications for Convective Strength and Structure, Monthly Weather Review, 143, 4355 – 4375, https://doi.org/10.1175/MWR-D-15-0154.1, https://journals.ametsoc.org/view/journals/mwre/143/11/mwr-d-15-0154.1.xml, 2015.

Lorenz, E. N.: The predictability of a flow which possesses many scales of motion, Tellus, 21, 289–307, https://doi.org/10.3402/tellusa.v21i3.10086, https://doi.org/10.3402/tellusa.v21i3.10086, 1969.

Mapes, B. E.: Gregarious Tropical Convection, Journal of Atmospheric Sciences, 50, 2026 – 2037, https://doi.org/10.1175/1520-0469(1993)050<2026:GTC>2.0.CO;2, https://journals.ametsoc.org/view/journals/atsc/50/13/1520-0469_1993_050_2026_gtc_2_0_co_2.xml, 1993.

McAnelly, R. L., Nachamkin, J. E., Cotton, W. R., and Nicholls, M. E.: Upscale Evolution of MCSs: Doppler Radar Analysis and Analytical Investigation, Monthly Weather Review, 125, 1083 – 1110, https://doi.org/10.1175/1520-0493(1997)125<1083:UEOMDR>2.0.CO;2, https://journals.ametsoc.org/view/journals/mwre/125/6/1520-0493_1997_125_1083_ueomdr_2.0.co_2.xml, 1997.

Melhauser, C. and Zhang, F.: Practical and intrinsic predictability of severe and convective weather at the Mesoscales, Journal of the Atmospheric Sciences, 69, 3350–3371, https://doi.org/10.1175/jas-d-11-0315.1, 2012.

Moncrieff, M. W.: Organized Convective Systems: Archetypal Dynamical Models, Mass and Momentum Flux Theory, and Parametrization, Quarterly Journal of the Royal Meteorological Society, 118, 819–850, https://doi.org/https://doi.org/10.1002/qj.49711850703, https://rmets.onlinelibrary.wiley.com/doi/abs/10.1002/qj.49711850703, 1992.

Morrison, H., Curry, J. A., and Khvorostyanov, V. I.: A New Double-Moment Microphysics Parameterization for Application in Cloud and Climate Models. Part I: Description, Journal of the Atmospheric Sciences, 62, 1665 – 1677, https://doi.org/10.1175/JAS3446.1, https://journals.ametsoc.org/view/journals/atsc/62/6/jas3446.1.xml, 2005.

Morrison, H., Thompson, G., and Tatarskii, V.: Impact of Cloud Microphysics on the Development of Trailing Stratiform Precipitation in a Simulated Squall Line: Comparison of One- and Two-Moment Schemes, Monthly Weather Review, 137, 991–1007, https://doi.org/10.1175/2008mwr2556.1, 2009.

Nicholls, M. E., Pielke, R. A., and Cotton, W. R.: Thermally Forced Gravity Waves in an Atmosphere at Rest, Journal of Atmospheric Sciences, 48, 1869 – 1884, https://doi.org/10.1175/1520-0469(1991)048<1869:TFGWIA>2.0.CO;2, https://journals.ametsoc.org/view/journals/atsc/48/16/1520-0469_1991_048_1869_tfgwia_2_0_co_2.xml, 1991.

Pandya, R. E. and Durran, D. R.: The influence of convectively generated thermal forcing on the mesoscale circulation around squall lines, Journal of the Atmospheric Sciences, 53, 2924–2951, https://doi.org/10.1175/1520-0469(1996)053lt;2924:tiocgtgt;2.0.co;2, 1996.

Rotunno, R., Klemp, J. B., and Weisman, M. L.: A theory for strong, long-lived squall lines, Journal of the Atmospheric Sciences, 45, 463–485, https://doi.org/10.1175/1520-0469(1988)045lt;0463:atfsllgt;2.0.co;2, 1988.

Selz, T.: Estimating the Intrinsic Limit of Predictability Using a Stochastic Convection Scheme, Journal of the Atmospheric Sciences, 76, 757–765, https://doi.org/10.1175/jas-d-17-0373.1, 2019.

Selz, T., Riemer, M., and Craig, G.: The transition from practical to intrinsic predictability of midlatitude weather, Journal of the Atmospheric Sciences, https://doi.org/10.1175/JAS-D-21-0271.1, https://journals.ametsocwe.org/view/journals/atsc/aop/JAS-D-21-0271.1/JAS-D-21-0271.1.xml, 2022.

Skamarock, W. C.: Evaluating mesoscale NWP models using kinetic energy spectra, Monthly Weather Review, 132, 3019–3032, https://doi.org/10.1175/mwr2830.1, 2004.

Stechmann, S. N. and Majda, A. J.: Gravity waves in shear and implications for organized convection, Journal of the Atmospheric Sciences, https://doi.org/10.1175/2009JAS2976.1, 2009.

Torn, R. D. and Romine, G. S.: Sensitivity of Central Oklahoma Convection Forecasts to Upstream Potential Vorticity Anomalies during Two Strongly Forced Cases during MPEX, Monthly Weather Review, 143, 4064 – 4087, https://doi.org/10.1175/MWR-D-15-0085.1, https://journals.ametsoc.org/view/journals/mwre/143/10/mwr-d-15-0085.1.xml, 2015.

Varble, A., Zipser, E. J., Fridlind, A. M., Zhu, P., Ackerman, A. S., Chaboureau, J.-P., Collis, S., Fan, J., Hill, A., and Shipway, B.: Evaluation of cloud-resolving and limited area model intercomparison simulations using TWP-ICE observations: 1. Deep convective updraft properties, Journal of Geophysical Research: Atmospheres, 119, 13,891–13,918, https://doi.org/https://doi.org/10.1002/2013JD021371, https://agupubs.onlinelibrary.wiley.com/doi/abs/10.1002/2013JD021371, 2014.

Varble, A., Morrison, H., and Zipser, E.: Effects of Under-Resolved Convective Dynamics on the Evolution of a Squall Line, Monthly Weather Review, 148, 289 – 311, https://doi.org/10.1175/MWR-D-19-0187.1, https://journals.ametsoc.org/view/journals/mwre/148/1/mwr-d-19-0187.1.xml, 2020.

Weisman, M. L. and Klemp, J. B.: The Dependence of Numerically Simulated Convective Storms on Vertical Wind Shear and Buoyancy, Monthly Weather Review, 110, 504–520, https://doi.org/10.1175/1520-0493(1982)110<0504:tdonsc>2.0.co;2, https://doi.org/10.1175/1520-0493(1982)110<0504:tdonsc>2.0.co;2, 1982.

Weisman, M. L. and Rotunno, R.: "A theory for strong long-lived squall lines" revisited, Journal of the Atmospheric Sciences, 61, 361–382, https://doi.org/10.1175/1520-0469(2004)061lt;0361:atfslsgt;2.0.co;2, 2004.

Weisman, M. L., Skamarock, W. C., and Klemp, J. B.: The resolution dependence of explicitly modeled convective systems, Monthly Weather Review, 125, 527–548, https://doi.org/10.1175/1520-0493(1997)125lt;0527:trdoemgt;2.0.co;2, 1997.

Weyn, J. A. and Durran, D. R.: The Dependence of the Predictability of Mesoscale Convective Systems on the Horizontal Scale and Amplitude of Initial Errors in Idealized Simulations, Journal of the Atmospheric Sciences, 74, 2191 – 2210, https://doi.org/10.1175/JAS-D-17-0006.1, https://journals.ametsoc.org/view/journals/atsc/74/7/jas-d-17-0006.1.xml, 2017.

Wilks, D. S.: "The Stippling Shows Statistically Significant Grid Points": How Research Results are Routinely Overstated and Overinterpreted, and What to Do about It, Bulletin of the American Meteorological Society, 97, 2263–2273, https://doi.org/10.1175/bams-d-15-00267.1, 2016.

Zhang, F.: Dynamics and structure of mesoscale error covariance of a winter cyclone estimated through short-range ensemble forecasts, Monthly Weather Review, https://doi.org/10.1175/MWR3009.1, 2005.

Zhang, F., Bei, N., Rotunno, R., Snyder, C., and Epifanio, C. C.: Mesoscale Predictability of Moist Baroclinic Waves: Convection-Permitting Experiments and Multistage Error Growth Dynamics, Journal of the Atmospheric Sciences, 64, 3579–3594, https://doi.org/10.1175/jas4028.1, https://doi.org/10.1175/jas4028.1, 2007.

Zhang, F., Sun, Y. Q., Magnusson, L., Buizza, R., Lin, S.-J., Chen, J.-H., and Emanuel, K.: What Is the Predictability Limit of Midlatitude Weather?, Journal of the Atmospheric Sciences, 76, 1077 – 1091, https://doi.org/10.1175/JAS-D-18-0269.1, https://journals.ametsoc.org/view/journals/atsc/76/4/jas-d-18-0269.1.xml, 2019.